E. Wolf, Progress in Optics 42

Chapter 6

Transverse mode shaping and selection in laser resonators

by

Ram Oron, Nir Davidson, Asher A. Friesem

Department of Physics of Complex Systems, Weizmann Institute of Science, Rehovot 76100, Israel

and

Erez Hasman

Optical Engineering Laboratory, Faculty of Mechanical Engineering, Technion – Israel Institute of Technology, Haifa 32000, Israel

Contents

§ 1. Introduction

One of the important properties of a laser is the transverse field distribution of the beam emerging from the laser resonator. This field distribution determines the divergence of the emerging beam and how well this beam can be focused. Due to diffraction, the field distribution is generally not uniform, but is a combination of discrete transverse patterns. Each pattern of the field distribution is related to a specific mode or a combination of modes that propagates inside the laser resonator. The transverse shape of the field distribution is maintained along the propagation path inside the resonator and after emerging from the laser.

Laser modes can be selected, controlled, and modified by inserting specially designed elements inside the resonator so as to obtain a desired laser output beam. These output beams from the laser could be further manipulated and shaped outside the resonator. The intra-cavity elements can tailor the field distribution of specific transverse modes, resulting in a field distribution which changes along the path inside the resonator, but returns to the original distribution after a round-trip of the resonator. Also, selection of specific transverse modes can be obtained by elements that introduce low losses to a specific desired mode, but high losses to other modes. In recent years, new fabrication technologies, most of which emerged from the semiconductor industry, enabled the realization and even mass production of intra-cavity elements with small feature size. This allowed the exploitation of new mode discrimination and mode shaping methods.

In this article, the basics of laser transverse modes are reviewed, along with numerical methods to calculate them. Various mode shaping and mode selection techniques are presented in detail, along with experimental data. Also, the output beam properties, as well as applications of specially designed beams, are discussed. Reviews of laser modes can be found in textbooks (see for example Siegman [1986] and Hodgson and Weber [1997]).

Section 2 describes transverse modes in stable and unstable resonators, as well as numerical and analytical methods to determine the field distributions of the transverse modes. Section 3 describes various methods to select specific transverse modes in laser resonators, along with techniques for fabricating the needed intra-cavity elements. The analytical tools for describing the properties

of the laser output beams, along with selected applications are presented in § 4. Finally, § 5 presents some concluding remarks.

§ 2. Transverse modes

Laser resonators are generally categorized as either stable or unstable. In a stable resonator, a ray launched inside the resonator parallel to the optical axis remains inside it, whereas in an unstable resonator, the ray may bounce off the resonator after a few round-trips. For example, a resonator of length L and mirror curvatures R_1 and R_2 is stable if $0 < (1 - L/R_1)(1 - L/R_2) < 1$, and unstable otherwise. Another important property of the resonator is the Fresnel number, given by $N_F = a^2/\lambda L$, where a is the resonator radius, and λ the operating wavelength. Hodgson and Weber [1997] introduced an equivalent Fresnel number, which is also dependent on the curvature of the mirrors. In such laser resonators, the transverse modes, each having a specific field distribution, should reproduce themselves after each round-trip. Such self-consistent field distributions could be determined by solving the round-trip wave propagation equation of the resonator. In this section, an introduction to transverse modes of both stable and unstable resonators is given, along with analytical methods of calculating them.

2.1. *Transverse modes in laser resonators*

The round-trip wave-beam propagation equations were solved in either circular or rectangular symmetry to yield the Laguerre–Gaussian and the Hermite–Gaussian transverse modes respectively (see Kogelnik and Li [1966] and Siegman [1986]). For cylindrical coordinates, TEM_{pl} Laguerre–Gaussian modes are characterized by p radial nodes and l angular nodes, whereas in Cartesian coordinates, TEM_{mn} Hermite–Gaussian modes are characterized by m and n modes in the horizontal and vertical directions respectively.

With circular symmetry, the field distribution $E(r,\theta)$ of a nondegenerate Laguerre–Gaussian $\mathrm{TEM}_{p,l}$ mode inside a laser resonator is expressed by

$$E_{p,l}(r,\theta) = E_0 \rho^{|l|/2} L_p^{|l|}(\rho) \exp(-\rho/2) \exp(\mathrm{i}l\theta), \tag{1}$$

where r and θ are the cylindrical coordinates, E_0 the magnitude of the field, $\rho = 2r^2/w^2$ with w the spot size of the Gaussian beam (see Hodgson and Weber [1997] for a detailed discussion), and L_p^l are the generalized Laguerre

polynomials of order p and index l (note that for nondegenerate modes, l may be positive or negative). Some specific values of the Laguerre polynomials are

$$\begin{aligned} &L_0^l(\rho) = 1, \quad L_1^l(\rho) = l + 1 - \rho, \\ &L_2^l(\rho) = \tfrac{1}{2}\rho^2 - (l+2)\rho + \tfrac{1}{2}(l+1)(l+2), \\ &L_p^l(\rho) = (-1)^l \partial^l / \partial \rho^l L_{p+l}(\rho). \end{aligned} \tag{2}$$

Now, modes with the same radial index p and opposite angular index l have the same radial distribution (albeit with opposite helical phases). They are usually degenerate, and appear simultaneously, leading to a TEM_{pl} (degenerate Laguerre–Gaussian) mode with

$$E_{pl}(r, \theta) = E_0 \rho^{l/2} L_p^l(\rho) \exp(-\rho/2) \cos(l\theta). \tag{3}$$

For clarity, a sign for the l value (e.g., $\mathrm{TEM}_{1,+2}$) will indicate the nondegenerate modes, and the degenerate modes (where l is always nonnegative), will appear without a sign (e.g., TEM_{12}). Note, in general, the intensity distribution of the $\mathrm{TEM}_{p,\pm l}$ modes will have a circularly symmetric annular shape, whereas those of the TEM_{pl} will have lobes, except for the fundamental, Gaussian-shaped TEM_{00} mode. Also, adjacent lobes will have opposite phases (π phase shift). The normalization factor for the $\mathrm{TEM}_{p,\pm l}$ mode is $\sqrt{\frac{p!}{\pi(p+|l|)!}}$, whereas for the TEM_{pl} mode it is $\sqrt{\frac{2p!}{(1+\delta_{0l})\pi(p+l)!}}$, with $\delta_{0l} = 1$ when $l = 0$ and $\delta_{0l} = 0$ otherwise.

Similarly, with rectangular symmetry, we obtain the TEM_{mn} Hermite–Gaussian modes, given by

$$E_{mn}(x, y) = E_0 \exp[-(\xi^2 + \psi^2)/2] H_m(\xi) H_n(\psi), \tag{4}$$

where x and y are the Cartesian coordinates, $\xi = \sqrt{2}\, x/w$, $\psi = \sqrt{2}\, y/w$, the normalization factor is $\sqrt{2/\pi}$ and the Hermite polynomials H are

$$\begin{aligned} &H_0(x) = 1, \quad H_1(x) = 2x, \quad H_2(x) = 4x^2 - 2, \\ &H_3(x) = 8x^3 - 12x, \quad H_4(x) = 16x^4 - 48x^2 + 12. \end{aligned} \tag{5}$$

Note, the Hermite–Gaussian (HG) modes with $m, n \leqslant 1$ are also Laguerre–Gaussian (LG) modes, namely,

$$\begin{aligned} &\mathrm{TEM}_{00}^{\mathrm{HG}} = \mathrm{TEM}_{00}^{\mathrm{LG}}, \quad \mathrm{TEM}_{01}^{\mathrm{HG}} = \mathrm{TEM}_{01(y)}^{\mathrm{LG}}, \\ &\mathrm{TEM}_{10}^{\mathrm{HG}} = \mathrm{TEM}_{01(x)}^{\mathrm{LG}}, \quad \mathrm{TEM}_{11}^{\mathrm{HG}} = \mathrm{TEM}_{02}^{\mathrm{LG}}, \end{aligned} \tag{6}$$

where the subscripts (x) and (y) denote the axis connecting the two lobes of the TEM_{01} mode, and correspond to cosine or sine functions in eq. (3), respectively.

Generally, in stable resonators, the number of modes existing in a resonator increases with the Fresnel number, as the width of the resonator increases and the losses of all modes decrease. The Fresnel number can be controlled either by changing the length of the resonator, or, most commonly, by inserting an aperture into the resonator and adjusting its radius. When the Fresnel number is small the laser operates with a single fundamental mode of Gaussian shape and lowest losses; when the Fresnel number is high, it operates with multi-transverse modes. Typically, a multimode laser operation results in a relatively poor beam quality. When a high-quality laser beam is required, one usually operates the laser with the fundamental mode. However, this concomitantly results in a significant decrease in output power, so there is a trade-off between output power and beam quality.

The unstable resonators are divided into two types, namely negative- and positive-branch, depending on the product $(1-L/R_1)(1-L/R_2)$, which is either negative or greater than unity, respectively. Negative-branch unstable resonators exhibit a focal spot in the resonator, at which there is an undesired high intracavity intensity, so they are less common. As for stable resonators, the modes of unstable resonators are determined by solving the round-trip propagation equation. However, in contrast to stable resonators, the beam propagation can be readily approximated by geometrical optics. Indeed, unstable resonators can be characterized, in the geometrical limit, by two spherical waves that reproduce themselves after each round-trip (see Siegman [1974]). In such resonators the round-trip waves diverge, resulting in magnification M. This leads to a round-trip mode loss of $1-(1/M)^2$.

A more precise determination of the mode losses and patterns requires solving the Kirchhoff integral directly. Siegman [1974] presented such solutions for various values of the Fresnel number, where he showed that the lowest loss mode depends on the Fresnel number. This is in contrast to stable resonators where the fundamental Gaussian mode has the lowest losses for every Fresnel number. Moreover, the power loss per pass is lower than expected from the geometrical approximation. This is attributed to diffraction effects that act to reshape the exact eigenmode in such a way as to reduce the losses below the geometrical value. Overall, unstable resonators with relatively large Fresnel numbers can operate with a single mode. Thus, they can have relatively high single mode output powers.

2.2. *Methods of analysis and design*

In this subsection, we describe analytical methods to determine the modes of

given resonator and intra-cavity elements that are needed to control or shape specific mode patterns. We begin with the round-trip propagation equation, given by

$$\boldsymbol{K}\boldsymbol{U}_n = \gamma_n \boldsymbol{U}_n, \tag{7}$$

where the eigenvectors $\boldsymbol{U}_n$ represent the field distribution of the resonator modes, the power loss per pass $1-|\gamma_n|^2$ is obtained from the eigenvalues γ_n and $\boldsymbol{K}$ represents the round-trip Kirchhoff propagation kernel. The free-space propagation is represented by the Kirchhoff–Fresnel integral (see Hodgson and Weber [1997] for details), whereas other intra-cavity elements, such as mirrors, lenses and phase elements are represented by appropriate operators, from which the round-trip operator $\boldsymbol{K}$ is obtained.

Solving eq. (7) is equivalent to the diagonalization of a matrix operator $\boldsymbol{K}$. However, when the matrix $\boldsymbol{K}$ is large, there could be a practical problem of diagonalizing it directly. In the following, several methods for solving eq. (7), as well as tailoring resonators for specific desired modes (eigenvectors $\boldsymbol{U}_n$), are presented.

2.2.1. Fox–Li

Probably the most commonly used method is the iterative Fox–Li method (Fox and Li [1962]). Here, one starts from an arbitrary field distribution (initial vector $\boldsymbol{U}=\boldsymbol{V}_0$) and propagates it back and forth in the resonator by applying repeatedly the round-trip propagation kernel $\boldsymbol{K}$, to obtain a sequence of vectors $\boldsymbol{V}_{m+1}=\boldsymbol{K}\boldsymbol{V}_m$. If the initial vector $\boldsymbol{V}_0$ is represented by a linear combination of the eigenvectors, namely, $\boldsymbol{V}_0=\sum_n a_n\boldsymbol{U}_n$, then consequently, the series of vectors $\boldsymbol{V}_m$ is given by $\boldsymbol{V}_m=\sum_n a_n\gamma_n^m\boldsymbol{U}_n$. If the eigenvalues are ordered so that $\gamma_1 \geqslant \gamma_2 \geqslant \gamma_3 \geqslant \cdots \geqslant \gamma_N$, then for large m values, the eigenvector of the fundamental mode $\boldsymbol{U}_1$ will be dominant, namely, $\boldsymbol{V}_m \approx a_1\gamma_1^m\boldsymbol{U}_1$, and γ_1 could be obtained by $\gamma_1 \approx \boldsymbol{V}_{m+1}/\boldsymbol{V}_m$. Thus, after typically tens or hundreds of iterations, only the lowest loss fundamental mode is obtained. A lower number of iterations is needed if the initial vector $\boldsymbol{V}_0$ is close to $\boldsymbol{U}_1$. However, for a multimode resonator, where $\gamma_1 \approx \gamma_2 \approx \gamma_3 \ldots$, a combination of all the modes, along with their common eigenvalue, is obtained.

When the modes $\boldsymbol{U}_n$ are orthogonal, the Fox–Li method can be extended to obtain the other modes, after finding the fundamental mode $\boldsymbol{U}_1$. This could be done by selecting a new initial vector $\boldsymbol{V}_0'$, which is orthogonal to $\boldsymbol{U}_1$ (the component along $\boldsymbol{U}_1$ could also be removed from other vectors in the series $\boldsymbol{V}_m$). In such a way, the second lowest-order mode is determined. This procedure is

then repeated for higher-order modes. Another method for finding several lowest-losses modes is the Prony method, described in detail by Siegman and Miller [1970].

2.2.2. Gerchberg–Saxton

The Gerchberg–Saxton method involves an iterative algorithm (Gerchberg and Saxton [1972]), with which one can calculate the field distribution at one location in the resonator based on the intensity or phase constraints in two locations. For example, for a given intensity distribution at the output and a certain phase constraint at the back mirror, one can determine the field distribution at any location in the resonator. This method is particularly useful for designing mode shaping elements that are inserted into the resonator (see for example Makki and Leger [1999]). A schematic diagram of the algorithm in a laser resonator configuration is presented in fig. 1. One starts with a field having a desired

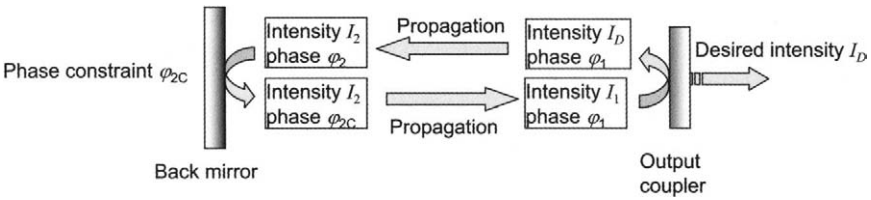

Fig. 1. Laser resonator configuration including the Gerchberg–Saxton algorithm with a desired intensity I_D at the output coupler and a phase constraint φ_{2C} at the back mirror.

intensity distribution I_D and random phase at the output coupler. This field propagates to the back mirror, to obtain $\sqrt{I_2}\exp(i\varphi_2)$. Then, a phase constraint is imposed so that the reflected field is $\sqrt{I_2}\exp(i\varphi_{2C})$. The phase constraint may directly depend on the incoming wave, such as for phase conjugation (see §§ 3.1 and 3.2), or perform a transformation from φ_2 to a uniform or spherical phase. This new reflected field distribution propagates back to the output coupler, resulting in $\sqrt{I_1}\exp(i\varphi_1)$, to which the intensity constraint I_D is applied again. This procedure is repeated, typically hundreds of times, until I_1 converges to I_D.

2.2.3. Propagation-matrix diagonalization

The propagation-matrix diagonalization method is based on directly solving the round-trip propagation equation (see eq. 7). This is done by first representing each of the intra-cavity elements (such as mirrors, apertures,

lenses and free-space propagation) with an appropriate matrix, then multiplying all matrices in the appropriate order to obtain the round-trip matrix. For example, for a simple resonator configuration with only two mirrors, $\boldsymbol{M}_{(\text{round-trip})} = \boldsymbol{M}_{(\text{free-space})} \cdot \boldsymbol{M}_{(\text{mirror1})} \cdot \boldsymbol{M}_{(\text{free-space})} \cdot \boldsymbol{M}_{(\text{mirror2})}$. Then, diagonalize the matrix $\boldsymbol{M}_{(\text{round-trip})}$ to find the eigenvectors $\boldsymbol{U}$, which represent the modes, and the eigenvalues γ, and thereby the round-trip losses.

Unlike the Fox–Li method, the propagation-matrix diagonalization method provides more detailed information on the number and shape of the individual modes in the resonator, and allows for a better physical insight. However, the propagation-matrix diagonalization method requires lengthy computations for the diagonalization, since the round-trip matrix is typically large. Some optimization of the computation is possible. For example, Sanderson and Streifer [1969] suggested an optimal procedure, which is based on a combination of two diagonalization techniques, yielding round-trip matrices of smaller size. Also, they compared between different methods of mode calculation, mainly, the Fox–Li method and several matrix diagonalization methods. Abrams and Chester [1974] optimized the diagonalization method for waveguide lasers. In both cases, the optimization is mainly based on the appropriate selection of a basis for describing the modes.

Oron, Danziger, Davidson, Friesem and Hasman [1999b] reduced the complexity of the analysis by exploiting the symmetry of the resonators. They selected a more general basis and considered a radially symmetric laser operating with Laguerre–Gaussian modes, so the analysis was reduced to one-dimensional (similar simplification was performed for Hermite–Gaussian modes by treating each of the Cartesian coordinates separately). Here, the free-space propagation was based on the Bessel–Fourier transformation, and could include various azimuthal field distributions, depending on the azimuthal index l (see also Ehrlichmann, Habich and Plum [1993]) to yield

$$U_l(r_2, L) = \mathrm{i}^{l+1} kL^{-1} \exp(-\mathrm{i}kL) \times \int U_l(r_1, 0) J_l(kr_1 r_2/L) \exp[-\mathrm{i}k(r_1^2 + r_2^2)/(2L)] r_1 \, \mathrm{d}r_1, \tag{8}$$

where $k = 2\pi/\lambda$. For every value of l, the integral in eq. (8) could also be represented by a matrix operator $\boldsymbol{M}_{l(\text{free-space})}$, namely, $\boldsymbol{U}_l(r,L) = \boldsymbol{M}_{l(\text{free-space})} \cdot \boldsymbol{U}_l(r,0)$. In a similar manner, each of the intra-cavity elements, such as mirrors, lenses or phase elements, can be represented by an appropriate matrix $\boldsymbol{M}$. Some representative results for a radially symmetric resonator are shown in fig. 2. Figures 2a–c show three sets of intensity distribution for the lowest order modes with azimuthal indices of $l = 0$, $l = 1$ or $l = 2$. Figure 2d shows the loss per pass

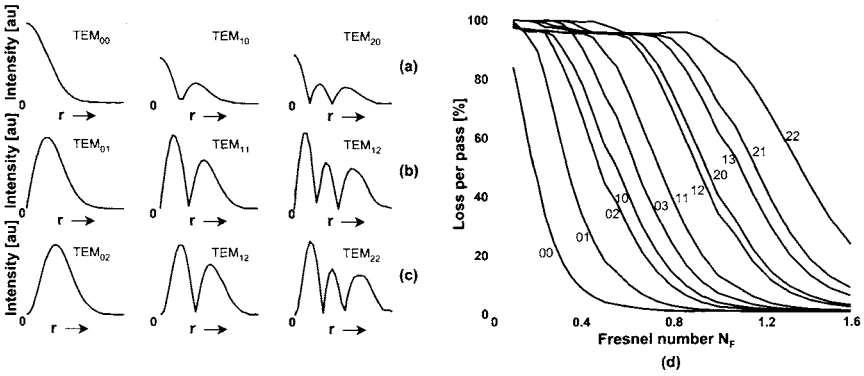

Fig. 2. Intensity distributions cross sections in the radial direction for Laguerre–Gaussian modes and their loss per pass as a function of N_F, (a) $l=0$, (b) $l=1$, (c) $l=2$, and (d) calculated mode losses as a function of N_F.

as a function of the Fresnel number N_F for these modes, which enables the prediction of the transverse mode content for a given Fresnel number and laser gain.

§ 3. Intra-cavity elements and resonator configurations

Intra-cavity elements can be incorporated into laser resonators in order to shape specific transverse mode patterns and to discriminate and select a specific single mode out of the many modes that exist in the resonator. Most mode-shaping methods modify the transverse field distribution of the lowest-order mode, from a Gaussian into another desired distribution such as a super-Gaussian or a nearly flat-top. Since the modified field distribution is no longer a mode of free space (that does not change as it propagates), the desired transverse field distribution is obtained only at a certain location in the resonator (for example, at the output coupler), whereas in other locations, the field distribution is different.

Most mode selection methods involve discrimination and selection of a specific "natural" (Laguerre–Gaussian or Hermite–Gaussian) single mode by introducing relatively high losses to all modes except the specific desired mode. While doing so, the desired mode will maintain the same transverse field distribution at all locations within the resonator. The simplest mode selection method involves the insertion of a circular aperture into the resonator in order to obtain the fundamental Gaussian mode. Other methods discriminate and select a specific high-order mode, introducing losses to all other modes including the

fundamental Gaussian mode. An early example of such a method was presented by Rigrod [1963], who isolated Laguerre–Gaussian modes in a laser resonator, by inserting wires into the resonator and adjusting the intra-cavity aperture diameter.

In this section, both mode shaping and mode selection techniques are described along with experimental results. These are based on various types of intra-cavity elements, including specially designed mirrors, diffractive elements, phase elements, and polarizing elements, that can be incorporated into both stable and unstable resonator configurations, to produce controlled output beams.

3.1. *Graded phase mirrors*

Graded phase mirrors (GPMs) have a nonspherical phase profile. The incorporation of such mirrors into laser resonators was proposed and analyzed by Bélanger and Paré [1991] (and Paré and Bélanger [1992]) in order to obtain a shaped (non-Gaussian) fundamental mode, with a predetermined field distribution at the output coupler. A resonator configuration with a GPM is presented in fig. 3. The output coupler is a plane mirror, whereas the back mirror is a GPM whose phase profile deviates from that of a spherical mirror of radius $r_0 = L$ by a phase shift of $\Delta\varphi$. By controlling this phase shift, one can shape the field distribution of the mode. In order to determine the phase profile of the GPM, one begins with a desired intensity distribution at the output coupler (the phase distribution at this point should be uniform). Then, this desired field propagates a distance of $L/2$, and the resulting phase distribution is found using the Kirchhoff–Fresnel diffraction integral. The phase profile of the GPM is then set as the conjugate of this phase, namely, a passive phase conjugate mirror for the desired mode.

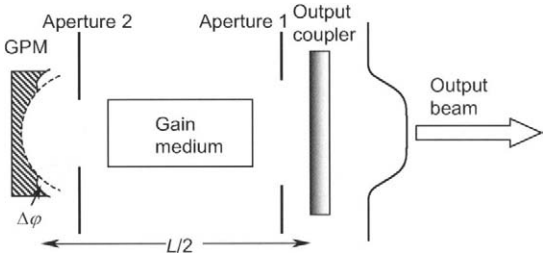

Fig. 3. Resonator configuration with a graded phase mirror (GPM). $\Delta\varphi$ is the phase difference between the GPM profile and a spherical mirror (dashed line) of radius $r_0 = L$. (From Paré and Bélanger [1992].)

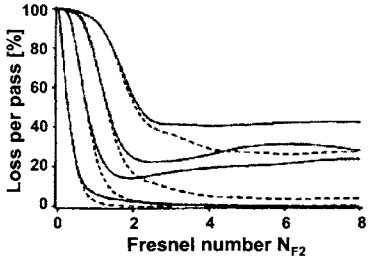

Fig. 4. Loss per pass $(1 - |\gamma|^2)$ as a function of the Fresnel number (N_{F2}) for the first four modes. Solid lines depict a 6th-order super-Gaussian resonator with a GPM; dashed lines depict a reference Gaussian resonator. (From Paré and Bélanger [1992].)

In order to obtain significant mode discrimination between the shaped fundamental mode and the higher order modes, the length of the laser resonator, $L/2$, should equal approximately the Rayleigh distance, namely $\pi w^2/\lambda$. With shorter resonators, the phase distribution at the back mirror is flat in the center and steep near the edges, leading to a complex GPM design and high alignment sensitivity. On the other hand, with longer resonators, the phase distribution is nearly spherical, so the phase shift $\Delta\varphi$ is very small, leading to decreased shaping ability.

A desired output intensity distribution for a GPM resonator could be a super-Gaussian of order n, given by

$$U(r) = \exp[-(r/w)^n]. \tag{9}$$

A high-order super-Gaussian mode has a nearly flat-top intensity distribution, which better fills the gain medium than a Gaussian mode, leading to higher output powers. Moreover, a laser operating with a super-Gaussian mode has a low loss for the fundamental mode and high losses for the higher order modes. These losses were calculated using the Prony method (see § 2.2), and the results for Gaussian and super-Gaussian modes are shown in fig. 4. As evident, with the GPM resonator, even for relatively high Fresnel numbers at aperture 2, there is significant mode discrimination between the fundamental and high-order modes, while maintaining low losses for the fundamental mode.

Bélanger, Lachance and Paré [1992] and Van Neste, Paré, Lachance and Bélanger [1994] performed experiments with a CO_2 laser in which GPMs were inserted in order to select super-Gaussian modes of orders 4 and 6, and compared the results to reference Gaussian modes. Figure 5 shows representative results of the laser output power as a function of aperture diameter, for a 6th-order super-Gaussian. Evidently, the output power first increases with aperture diameter

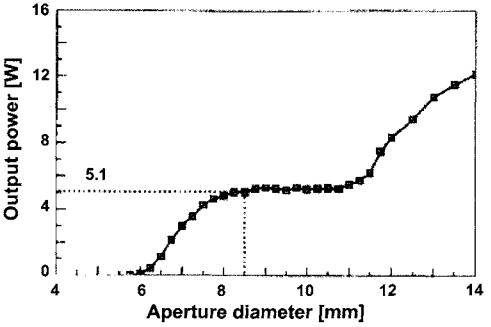

Fig. 5. Output power as a function of aperture diameter for a 6th-order super-Gaussian resonator with a GPM. (From Van Neste, Paré, Lachance and Bélanger [1994].)

to reach a plateau of approximately 5.1 W for a single-mode operation at an aperture diameter of 8 to 11 mm. The corresponding Gaussian output power was only 4.3 W, indicating a power increase of approximately 20% with the super-Gaussian. For larger aperture diameters, a multimode operation with higher output powers is obtained.

Angelow, Laeri and Tschudi [1996] showed that by applying a simulated-annealing optimization algorithm, it is possible to design GPMs with higher modal selectivity than obtained with the phase conjugation approach. However, this concomitantly implies somewhat higher fundamental mode losses. Pääkkönen and Turunen [1998] designed and analyzed resonator configurations with graded phase (aspheric) mirrors, which operate with Bessel–Gauss modes, and compared their mode losses with those of other Bessel–Gauss resonators.

3.2. *Diffractive elements*

Diffractive optical elements can transform one wavefront into another, so they are potentially useful for mode shaping. Leger, Chen and Wang [1994] replaced the back mirror in a laser resonator with a diffractive mirror in order to shape the mode intensity distribution. This mirror, designed in a similar manner to passive phase conjugate GPMs, is nearly flat and has a maximal phase variation of 2π, so the phase profile includes many 2π steps. The diffractive mirror was designed to form a square 20th-order super-Gaussian mode, and was incorporated into an Nd:YAG laser resonator. The experimental output profile results are shown in fig. 6. A nearly flat-top square was obtained, as expected for a super-Gaussian profile.

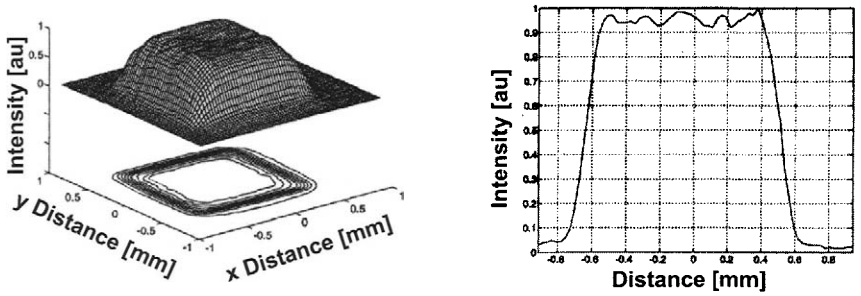

Fig. 6. Measured output intensity profile from an Nd:YAG laser with a diffractive mirror. (From Leger, Chen and Wang [1994].)

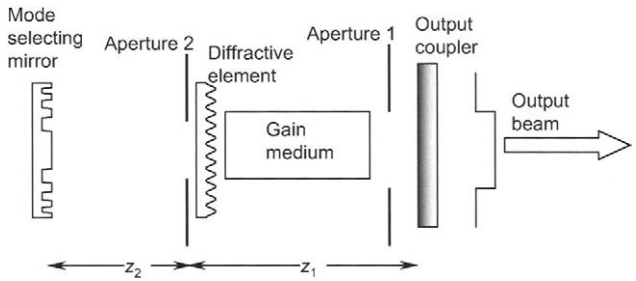

Fig. 7. Resonator configuration with a flat output coupler, a diffractive back mirror, and an additional intra-cavity diffractive element. (From Leger, Chen and Dai [1994].)

As for the laser resonator with a GPM, the length of the resonator with a diffractive mirror should be comparable to the Rayleigh distance. Thus, relatively long resonators are required. Leger, Chen and Dai [1994] proposed and demonstrated the insertion of an additional intra-cavity diffractive grating, which allows for high modal discrimination, yet with shorter resonator lengths. A typical resonator configuration is shown in fig. 7. The output mirror is simply flat, the back mirror is a diffractive mirror, and the internal diffractive phase grating is placed approximately in the middle of the resonator. The diameters of two apertures in the resonator are so chosen that negligible loss is introduced to the fundamental mode, but high losses to other modes. Typically, the internal diffractive element is a sinusoidal phase grating of the form $\exp[im \sin(2\pi f_g x]$, where m is the modulation index and f_g is the spatial frequency of the grating. Figure 8 shows the calculated modal threshold gain (given by $1/|\gamma|^2$) for the second-order mode in a specific resonator geometry, whereas for the fundamental mode it is nearly unity; for higher-order modes the threshold gain would of course be higher, so it need not be considered. As evident, the modal

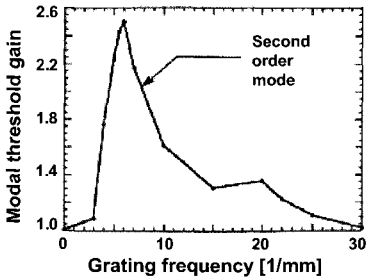

Fig. 8. Calculated modal threshold gain for the second order mode, for a laser with an internal diffractive sinusoidal grating. (From Leger, Chen and Dai [1994].)

threshold gain, which indicates the modal discrimination, is low for very low and very high grating frequencies, but reaches a maximum of approximately 2.5 at a grating frequency $f_g \approx 6\,\mathrm{mm}^{-1}$. This could be understood by considering the field at the diffractive mirror. This field consists of a multiplicity of near-field patterns resulting from several different orders of the internal grating that are separated by $\lambda z_2 f_g$. For very low grating frequencies (typically $f_g < 3\,\mathrm{mm}^{-1}$), the patterns greatly overlap, leading to relatively low mode discrimination. For very high grating frequencies (typically $f_g > 10\,\mathrm{mm}^{-1}$), there is little, if any, overlap, leading to relatively low mode overlap between the diffraction patterns, again leading to very low mode discrimination. For moderate grating frequencies (typically $3\,\mathrm{mm}^{-1} < f_g < 10\,\mathrm{mm}^{-1}$) there is partial overlap between the diffraction patterns, and mode discrimination becomes effective. With such mode discrimination, it is possible to obtain output with a super-Gaussian profile from a relatively short laser resonator.

Chen, Wang and Leger [1995] also investigated laser resonators with diffractive mirrors that operate with single high-order modes. The high-order modes were selected by inserting wires into the resonator, so as to introduce high losses and suppress the fundamental and low-order modes, while hardly affecting the loss of the desired high-order mode. The second-order mode was obtained by inserting a single wire along the y-axis, leading to a mode corresponding to the TEM_{01} mode. Some representative results are shown in figs. 9 and 10. Figure 9 shows the near- and far-field intensity distributions of the output beam. The nearly zero intensity in the center in both the near- and far-field patterns indicates that the two lobes have opposite phases. Similarly, by inserting another wire along the x-axis, a mode corresponding to the Hermite–Gaussian TEM_{11} mode (or the Laguerre–Gaussian TEM_{02} mode) was obtained. Figure 10 shows the measured modal threshold gain (given by $1/|\gamma|^2$) for the fundamental mode and

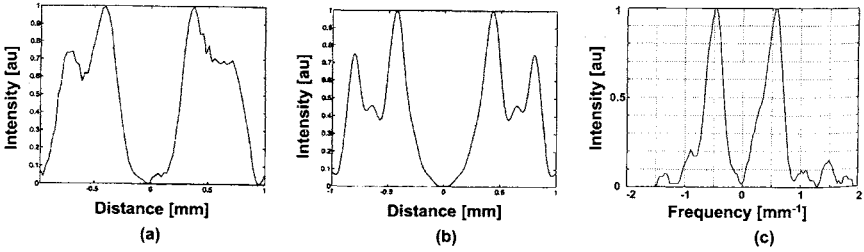

Fig. 9. Intensity distribution and cross sections for a laser operating with a wire to select the second order mode (denoted TEM_{01}): (a) experimental near-field intensity distribution; (b) calculated near-field cross section; (c) experimental far-field cross section. (From Chen, Wang and Leger [1995].)

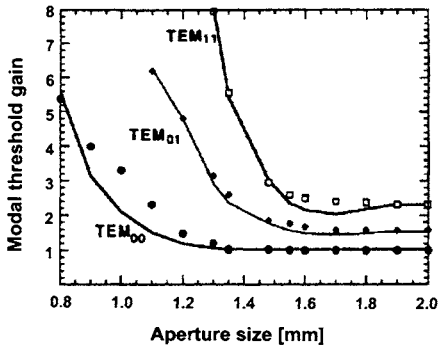

Fig. 10. Measured modal threshold gain of the fundamental (denoted TEM_{00}) and two higher-order modes (denoted TEM_{01} and TEM_{11}), as a function of output aperture diameter. Note, these modes are not the Hermite–Gaussian modes, but specific to the super-Gaussian resonator. (From Chen, Wang and Leger [1995].)

the two higher-order modes as functions of the aperture diameter. Evidently, high modal discrimination can be obtained.

Leger, Chen and Mowry [1995] also analyzed a pseudorandom phase plate internal diffractive element. The pseudorandom phase plate was designed with the Gerchberg–Saxton method to have a high bandwidth, so as to obtain higher mode discrimination than with the sinusoidal phase grating. Such pseudorandom phase plates are generally difficult to realize and more sensitive to misalignment. Napartovich, Elkin, Troschieva, Vysotsky and Leger [1999] suggested an internal diffractive element having the form of a simple phase step. Calculations showed that high modal discrimination with low fundamental-mode losses could be maintained. Lin and Wang [2000] analyzed laser resonators in which one of the mirrors was flat in the center, and had sinusoidal phase grating at the edges. By properly choosing the size of the central region and the spatial frequency of

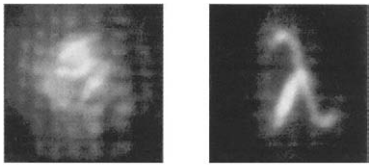

Fig. 11. Near- and far-field experimental results for a laser designed to produce a "λ" intensity distribution at the far field. (From Zeitner, Wyrowski and Zellmer [2000].)

the phase grating, a nearly flat-top output beam with uniform phase could be obtained.

Zeitner, Wyrowski and Zellmer [2000] investigated a different approach in order to obtain a desired laser output intensity distribution at the far field. They replaced the back mirror of the laser resonator with a diffractive mirror, in order to obtain an intensity distribution which is the Fourier transformation of the desired distribution. In order to introduce the appropriate phase to the emerging output beam (which has a uniform phase), another external phase element was placed adjacent to the output coupler. The far-field pattern was then simply obtained by a lens. The experimental results for the near and far fields are shown in fig. 11. A λ-shaped far-field pattern is obtained, albeit with some blurring effects attributed to inhomogeneous pumping and nonlinear effects.

3.3. *Binary phase elements*

Phase elements can change the phase distribution of an incident beam, just as diffractive elements can. The feature sizes in phase elements are significantly larger than those in diffractive elements, thereby alleviating fabrication concerns. In this subsection, mode-selecting binary phase elements, which consist of only two phase levels, are described along with experimental results in different resonator configurations.

The simplest method to selectively attenuate certain regions of the intensity distribution of a mode and thereby discriminate it from other modes is to insert some absorbing elements such as wire grids into the laser resonator. Such elements introduce losses by absorption, and they heat up, so they are relatively inefficient. Better efficiency can be obtained with non-absorbing phase elements that introduce the desired losses by diffraction and interference. Hence, we consider how binary phase elements can be exploited to introduce losses to

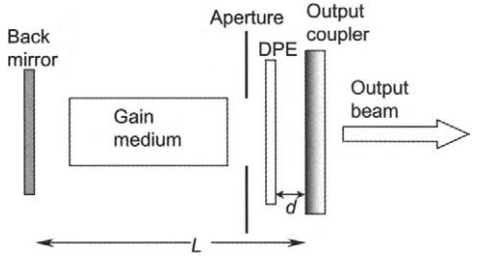

Fig. 12. Laser resonator configuration with a DPE inserted next to the output coupler.

specific modes, to discriminate between many modes, and to select one that will exist in the laser resonator.

Kol'chenko, Nikitenko and Troitskii [1980] replaced the absorbing wires by phase-shifting masks in order to select high-order transverse modes. The phase-shifting masks were designed to have a nearly π phase shift along narrow lines instead of wires, while no phase shift was introduced to other areas. These phase masks were found to introduce relatively low losses to the desired mode, while introducing high losses to other modes. Moreover, the mode discrimination was higher compared to wires.

Different and more general binary phase elements, useful for selecting only one desired high-order transverse mode, were developed by Oron, Danziger, Davidson, Friesem and Hasman [1999a]. They inserted binary discontinuous phase elements (DPEs), designed to match the phase distribution and selectively reverse the phases of the desired mode. Because DPEs have a specific phase distribution with sharp phase changes, the insertion of DPEs into the laser resonator results in minimal losses for a desired transverse mode but high losses to others.

Typically, the DPE is inserted near one of the resonator mirrors, preferably near the output coupler, as shown in fig. 12. The DPE is designed to ensure that discontinuous phase changes of either 0 or π occur at the interfaces between adjacent parts of a desired mode distribution, where the intensity is very low. Specifically, the DPE designed to select the azimuthal index l introduces an angular-dependent phase shift, of the form

$$\varphi(r,\theta) = \begin{cases} 0 & 3\pi/2 + 2\pi m > l\theta > \pi/2 + 2\pi m, \\ \pi & 5\pi/2 + 2\pi m > l\theta > 3\pi/2 + 2\pi m. \end{cases} \quad m \text{ integer.} \tag{10}$$

Note that for every (positive) value of l, a singular point appears in the origin of the DPE, which corresponds to the zero intensity in the origin for a TEM_{pl} mode with $l \neq 0$. DPEs could also be designed to select the radial index p. Some

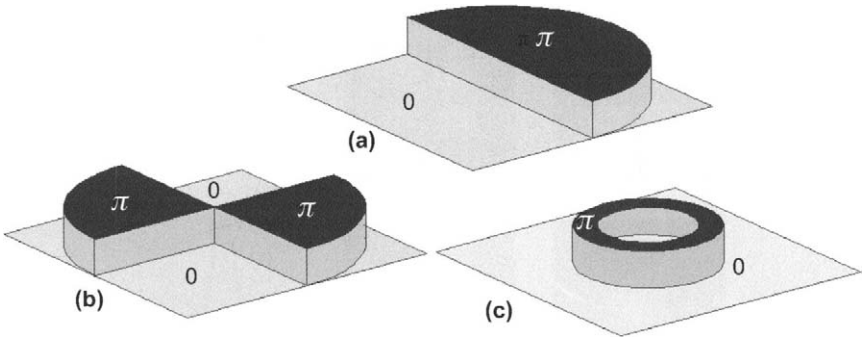

Fig. 13. Representative DPEs: (a) designed to select TEM_{01}; (b) designed to select TEM_{02}; (c) designed to select TEM_{20}.

representative DPEs, for selecting the TEM_{01}, TEM_{02} or TEM_{20} modes, are shown in fig. 13.

As a result of passing through the DPE, adjacent spots and adjacent rings of the field distribution in the desired mode, which normally have opposite phases (π phase shift), will now have the same phase. The output mirror then reflects the modified mode distribution so it passes once more through the DPE, and all parts of the mode field distribution revert back to their original values. This is due to the fact that the total phase change introduced by the DPE is 0 or 2π.

If the distance d between the DPE and the mirror is sufficiently short compared to the resonator length L (i.e., $d \ll L$), then the overall distribution of the desired mode does not change as it passes through the DPE twice in a round-trip. Specifically, the phase change introduced by the first passage is canceled by the return passage. However, all other modes, whose intensity distributions are different, suffer a sharp phase change at locations where their intensity is typically strong. Since $d \gg \lambda$, this leads to a strong divergence, where the phase change introduced by the first passage through the DPE is no longer canceled by the phase change introduced by the return passage. As a result, all modes except the desired mode suffer a loss, and most, if not all, are suppressed. Some modes, which are higher harmonics of the desired mode, may be unaffected by the DPE, but could easily be suppressed by a simple aperture. Finally, by placing the DPE next to the output coupler (as in fig. 12), all parts of the desired mode distribution are in phase, so that the far field of the output beam intensity has a high central peak, with some side-lobes.

Several theoretical and experimental representative results are presented in figs. 14–17. Figure 14 shows results with an Nd:YAG laser in which a DPE designed to select the TEM_{02} mode (such as shown in fig. 13b) was inserted next

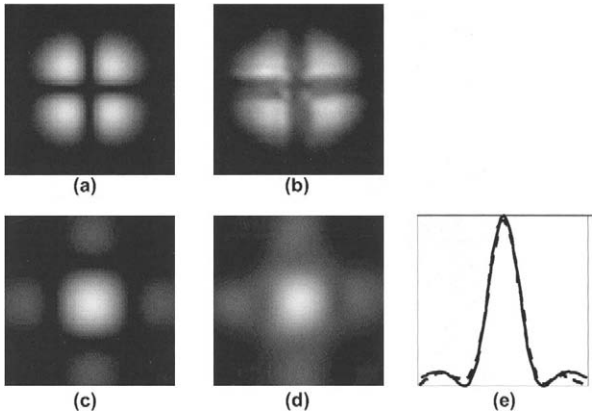

Fig. 14. Theoretical and experimental intensity distributions that emerge from an Nd:YAG laser in which a DPE was incorporated to obtain the TEM_{02} mode: (a) theoretical near field; (b) experimental near field; (c) theoretical far field; (d) experimental far field; and (e) theoretical (solid line) and experimental (dashed) cross sections along the center of the far fields. (From Oron, Danziger, Davidson, Friesem and Hasman [1999a].)

to the output coupler. The DPEs were formed by means of photolithographic and etching processes on fused silica, and antireflection (AR) coated. The length of the resonator was 60 cm. Figure 14a shows the theoretical near-field intensity distribution as calculated by eq. (3). The corresponding experimental near-field intensity distribution detected with a CCD camera is shown in fig. 14b. Both show the expected four lobes. Figure 14c shows the theoretical far-field intensity distribution obtained after applying a Fourier transformation acting on the absolute value of the near-field distribution (i.e., all four lobes are in phase). Figure 14d shows the corresponding experimental far-field intensity distribution. Finally, fig. 14e shows the corresponding central cross-sections of the far-field intensity distributions. As evident, there is a strong central peak, indicating that all four lobes of the near-field distribution are in phase. Using the DPE to make the laser operate with the TEM_{02} mode, the output power was 3.5 W, with an internal aperture set at $a = 1.1$ mm (i.e., $N_F = 1.9$). This was higher than the output power from the laser operating with the single fundamental mode (TEM_{00}), which was obtained by reducing the initial aperture to $a = 0.7$ mm (i.e., $N_F = 0.77$).

In a similar manner, the Laguerre–Gaussian TEM_{03} and TEM_{04} modes were selected. The near- and far-field intensity distributions from a laser operating with these modes are shown in fig. 15. Here again, we note the many lobes in the near field and a high central peak in the far field. Single high-order modes

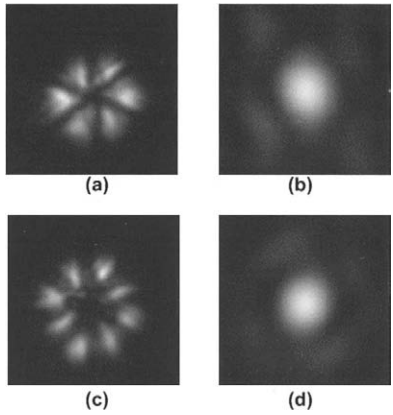

Fig. 15. Experimental intensity distributions that emerge from an Nd:YAG laser: (a) TEM_{03} near field; (b) TEM_{03} far field; (c) TEM_{04} near field; (d) TEM_{04} far field.

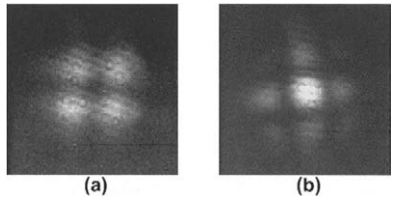

Fig. 16. Experimental intensity distributions that emerge from a pulsed (q-switched) Nd:YAG laser in which a DPE was incorporated to obtain the TEM_{02} mode: (a) near field; (b) far field.

were also obtained with a lamp-pumped Nd:YAG laser which was pulsed by applying electro-optical Q-switching. Results for the TEM_{02} mode operation, with an output energy of 15 mJ per pulse, are shown in fig. 16. In comparison with the fundamental Gaussian mode operation, the output energy was less than 10 mJ per pulse.

Figure 17 shows results from a CO_2 laser with a DPE inserted to select the TEM_{01} mode (such as shown in fig. 13a). Figure 17a shows the theoretical near-field intensity distribution, which was calculated by eq. (3). Figure 17b shows the corresponding experimental intensity distributions obtained with a pyroelectric camera. Both results show the expected two lobes. Figures 17c,d show the theoretical and experimental far-field intensity distributions, with a high central peak and two low side-lobes. Finally, fig. 17e shows the corresponding central cross-sections of the far-field intensity distributions. Inserting an internal aperture set at $a = 4$ mm (i.e., $N_F = 2.5$), an output power of 3.7 W was obtained, with 80% of the power concentrated in the central lobe. This was higher by more

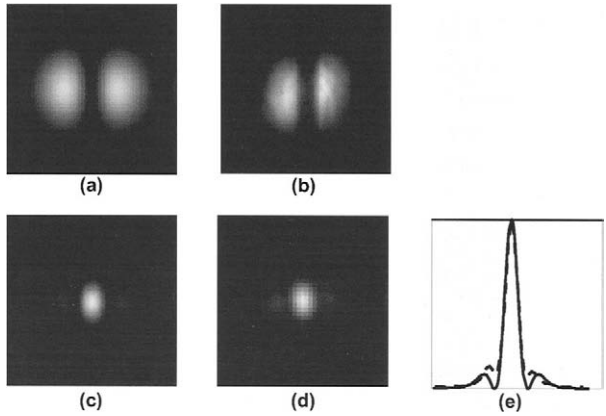

Fig. 17. Theoretical and experimental intensity distributions that emerge from a CO_2 laser in which a DPE was incorporated to obtain the TEM_{01} mode: (a) theoretical near field; (b) experimental near field; (c) theoretical far field; (d) experimental farfield; and (e) theoretical (solid line) and experimental (dashed) cross sections along the center of the far fields. (From Oron, Danziger, Davidson, Friesem and Hasman [1999a].)

than 50% than the output power of the single fundamental mode (TEM_{00}), which was obtained by reducing the aperture to $a = 3.4$ mm (i.e., $N_F = 1.8$).

The performance of the DPEs was compared to that of absorbing wires of various thicknesses. The maximal single-mode TEM_{01} power of the CO_2 laser, obtained for a wire diameter of 75 μm, was 20% lower than with the DPE, confirming the advantage of the phase elements.

3.4. *Spiral phase elements*

Spiral phase elements (SPEs) introduce a phase shift of $\exp(iN\theta)$, where θ is the azimuthal angle, to the beam passing through them. Representative examples of SPEs are shown in fig. 18. Figure 18a shows an SPE with $N = 1$, and

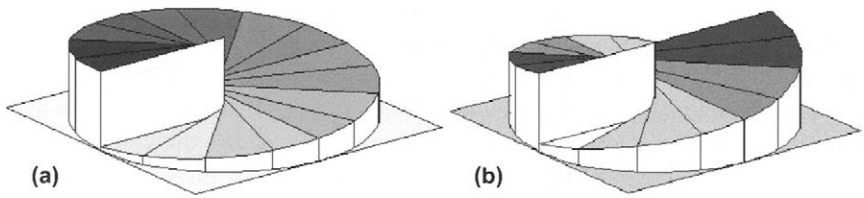

Fig. 18. Spiral phase elements (SPEs) with (a) $N = 1$ and (b) $N = 2$. The height discontinuities represent 2π phase shifts.

fig. 18b shows an SPE with $N=2$, where N represents the number of 2π phase discontinuities. The height discontinuities needed to obtain a 2π phase shift per passage (4π phase shift in reflection) are λ for a reflective element and $\lambda/(n-1)$ for a transmittive element (n is the refractive index). As evident, phase singularities appear in the origin of the SPEs.

Beijersbergen, Coerwinkel, Kristiansen and Woerdman [1994] exploited SPEs in order to transform Gaussian beams into helical beams outside the laser resonator. This transformation generally results in a combination of helical beams of different helicity. For example, a Gaussian beam incident on an SPE with $N=1$ results in 78% of the power in a $TEM_{0,+1}$ beam, and the rest of the power in other high-order helical beams. The degradation in efficiency is attributed to different intensity distributions of the original and transformed beams, so in general, the efficiency is higher as the intensity distribution of the original and transformed beams are closer, and it could reach 100% for beams having the same intensity distribution (such as the $TEM_{0,+1}$ and $TEM_{0,-1}$).

A helical mode can be formed inside a laser resonator, so a helical beam would emerge directly from the laser. Harris, Hill, Tapster and Vaughan [1994] exploited a helical laser mode operation based on coherent intra-cavity coupling and summation of two nonhelical modes. Sherstobitov and Rodionov [2000] proposed to apply SPEs in order to select helical modes in unstable resonators. In this case the SPE replaces the output coupler mirror, and a curved roof reflector serves as the back mirror. Calculations predicted that the emerging beam is indeed nearly helical.

Oron, Danziger, Davidson, Friesem and Hasman [1999b] applied SPEs inside laser resonators in order to discriminate and select high-order helical Laguerre–Gaussian modes. In this approach, based on azimuthal mode discrimination, the SPEs are essentially lossless for the desired high-order mode, but introduce high losses to all other modes, especially to the fundamental Gaussian mode. The mode discrimination removes the degeneracy and separates helical modes with opposite l (angular momentum). The SPEs, in essence, change the phase of a wavefront passing through them, in accordance to either $\exp(+iN\theta)$ or $\exp(-iN\theta)$.

Three laser resonator configurations with SPEs are shown schematically in fig. 19. Figure 19a shows the basic laser resonator configuration with the two SPEs adjacent to the resonator mirrors. Alternatively, reflective SPEs can replace the mirrors. The first SPE changes the angular mode index of the mode passing through it twice by $-2N$, i.e., the mode of angular index l changes to $l-2N$ and the second SPE changes it back to l. With these SPEs the modes with an angular index of $l=+N$ will be changed to those with $l=-N$. As a result,

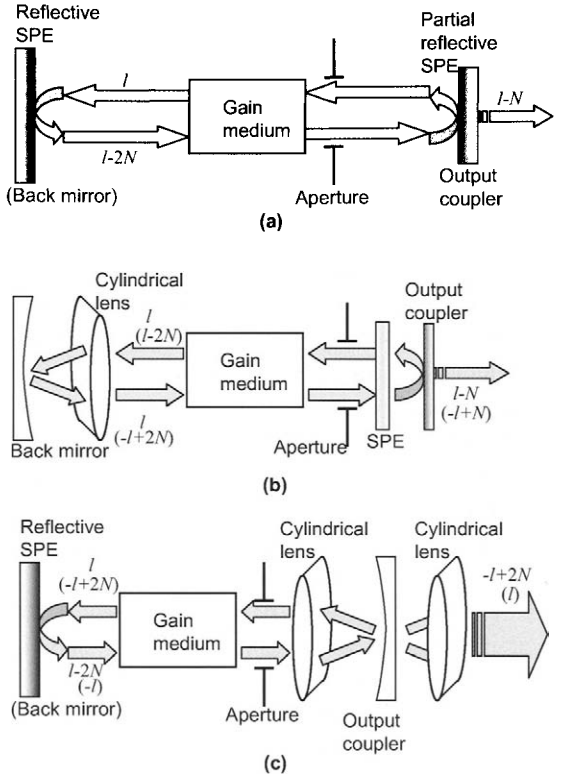

Fig. 19. Laser resonator configurations with SPEs: (a) a configuration with two SPEs, each placed adjacent to a laser mirror; (b) a configuration with a single SPE, placed next to the output coupler, and a cylindrical lens (which reverses the angular phase) focused on the back mirror; (c) a configuration with an added external cylindrical lens, to form helical beams. The angular indices are indicated along the round-trip (second trip in parentheses).

since modes of opposite l have the same intensity distribution, only these modes will maintain the same distribution before and after passing through the SPEs. However, the radial distribution for the other modes will have the form of a combination of Laguerre–Gaussian modes, each with a different angular index l, so they will be wider, and the losses for all modes having $l \neq N$ will be higher. Thus, in accordance to the design of the SPEs, it is possible to select a specific mode that will propagate inside the laser resonator. Moreover, it is possible to separate two $TEM_{p,\pm l}$ modes with opposite angular indices, so as to lead to a pure $TEM_{p,+l}$ distribution. Specifically, the mode will be linearly polarized with a field distribution of the form given by eq. (1), i.e., doughnut-shaped, rather

than that of TEM_{pl} of the form in eq. (3), i.e., a distribution with distinct and separate lobes.

Figure 19b shows a laser resonator configuration in which one of the SPEs is replaced by an element that reverses the angular phase (such as a cylindrical lens focused on the resonator mirror, or a Porro prism). In this configuration, each passage through the SPE changes the angular index of the mode passing through it by $-N$, and the angular phase-reversing element simply reverses the sign of the angular index. Here again, the Laguerre–Gaussian radial distribution is maintained after each round-trip only for those modes having an angular index $l=N$. For other modes, however, the radial distribution is wider, resulting in significantly higher losses. As evident from figs. 19a,b, the emerging laser beam passes through the SPE only once. As a result, the phase distribution of the output beam is constant. Thus, it converges to a relatively small single lobe in the far field, with no need for any external element. This concomitantly leads to an improvement in M^2, as will be discussed in sect. 4.

Alternatively, by replacing the back mirror with an output coupler and adding an external cylindrical lens (fig. 19c), it is possible to obtain the internal mode pattern outside the laser. Such configuration was applied by Oron, Davidson, Friesem and Hasman [2000b] to form pure helical beams. This could also be obtained by inserting a beam splitter inside the resonator so it will serve as an output coupler for getting the internal beam out of the resonator. Here, the back mirror is replaced with a reflective SPE, which changes the phase of the wavefront upon reflection by $\exp(+2iN\theta)$ for a desired helical mode with $l=N$. Thus, a helical mode with phase $\exp(-il\theta)$ is converted into $\exp(+il\theta)$ after reflection by the SPE. The cylindrical lens, which is located inside the resonator and focused on the output coupler, inverts the helicity of the mode back to $\exp(-il\theta)$ after a round-trip, to ensure self-consistency of the desired helical mode. The beam emerging from the resonator is collimated by another external cylindrical lens, so its distribution will have the same form as the intra-cavity helical mode pattern. Note that the helicity of the SPE determines the helicity of the helical mode in the laser resonator. Consequently, by designing the SPE with a specific helicity, it is possible to control the helicity of the helical beam emerging from the laser.

In all three configurations, the insertion of an aperture inside the resonator ensures that the laser operates with the lowest-order helical mode, i.e., $TEM_{0,+l}$. In order to determine the aperture diameter, the mode discrimination for such resonator configurations was calculated by the matrix-diagonalization method. Due to the circular symmetry of the resonator, the usually complex matrices, based on Bessel–Fourier transformation, become simpler (see sect. 2.2.3). The

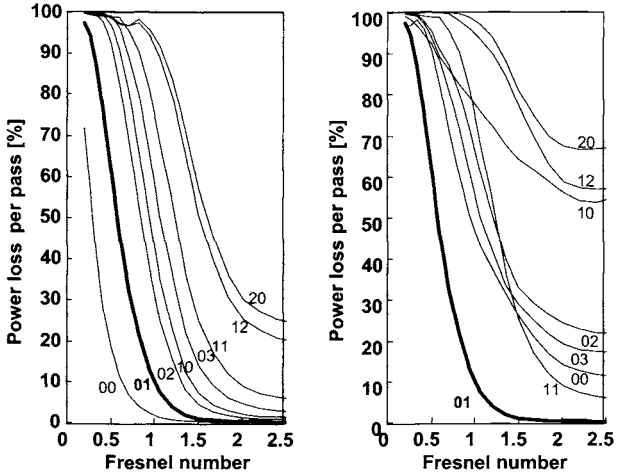

Fig. 20. Diffraction losses in a round-trip for various Laguerre–Gaussian transverse modes as a function of the Fresnel number $N_F = a^2/\lambda L$. The bold curves represent the $TEM_{0,+1}$ mode: (a) laser configuration with no SPEs; (b) laser configuration with a single SPE of $N = 1$ and a phase reverting element, inserted into the resonator. (From Oron, Danziger, Davidson, Friesem and Hasman [1999b].)

calculated results are presented in fig. 20. The power loss per round-trip as a function of the Fresnel number N_F is shown for the different modes in the laser resonator. Figure 20a shows the losses for a laser resonator configuration without any SPEs, whereas fig. 20b shows the losses for a configuration with one SPE of $N = 1$, and a phase-reversing element. Evidently, the losses of the modes with $l = 1$ are not affected by the SPE, while all other modes (including the fundamental TEM_{00} mode) suffer very high losses. Thus, laser operation with a single high-order mode can be obtained with a Fresnel number of approximately 2, which is significantly larger than that of a laser operating with the fundamental Gaussian mode.

An SPE was incorporated into a CO_2 laser resonator configuration with a cylindrical lens, such as shown in fig. 19b. The laser was a discharge-pumped CO_2 laser whose length was 60 cm, the SPE was formed for $N = 1$ on GaAs substrates by means of a 16-level photolithographic process and the cylindrical lens of ZnSe had a focal length of 7.5 cm. The SPE and the cylindrical lens had AR coating for $\lambda = 10.6\,\mu m$. A variable aperture, inside the laser resonator, was adjusted until the emerging beam contained only one mode, leading to a Fresnel number of 2.

The results are shown in fig. 21, along with the corresponding calculated results from eq. (1). Figure 21a depicts the calculated laser output near-

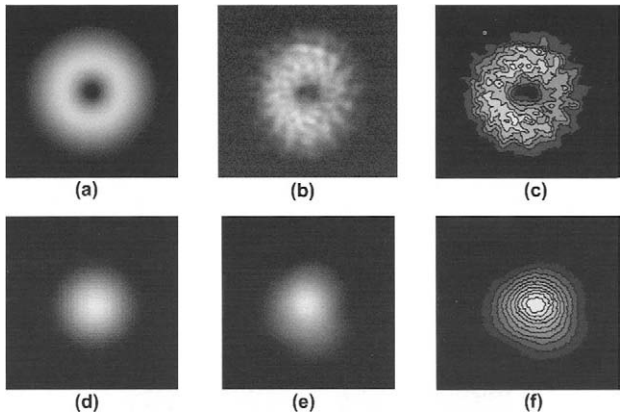

Fig. 21. Theoretical and experimental intensity distributions that emerge from a CO_2 laser in which a SOE with $N = 1$ was incorporated to obtain the $TEM_{0,+1}$ mode: (a) theoretical near field; (b, c) experimental near field; (d) theoretical far field; (e, f) experimental far field. (From Oron, Danziger, Davidson, Friesem and Hasman [1999b].)

field intensity distribution corresponding to the $TEM_{0,+1}$ mode. Figures 21b,c present the corresponding experimental near-field pattern and contour plot. The expected doughnut-shape distribution is clearly evident in both calculated and experimental results. The nonuniformities in the experimental distribution arise from the 16-level discontinuities, caused by the $\pi/8$ phase steps. Figure 21d depicts the theoretical far-field laser output intensity distribution, which is calculated by the Fourier transformation of the near-field pattern with a uniform phase. Figures 21e,f depict the corresponding experimental far-field pattern and contour plot. The excellent agreement between the theoretical and experimental far-field patterns is evident, indicating that all parts of the near-field pattern are in phase.

Also, opening the aperture to allow for higher-order transverse mode operation, and carefully adjusting the resonator length L so as to control the longitudinal modes, lead to laser operation with high-order modes. This is attributed to the coupling between longitudinal and transverse modes in such a CO_2 laser. The laser output near-field intensity distributions corresponding to these higher modes are shown in fig. 22. As evident, the helical phase causes spiral-like patterns, and the higher the mode order, the higher number of lobes in the laser output near-field intensity distributions.

SPEs were also incorporated into an Nd:YAG laser resonator. The laser resonator configuration included two SPEs, as shown in fig. 19a. The laser was a flashlamp-pumped Nd:YAG laser whose length was 60 cm, and both

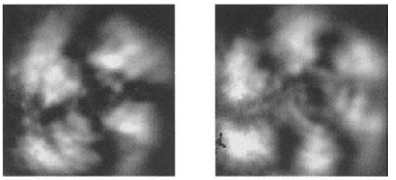

Fig. 22. Near-field intensity distributions corresponding to higher-order modes in a resonator with a SPE: (a) second-order mode with four lobes; (b) third-order mode with six lobes.

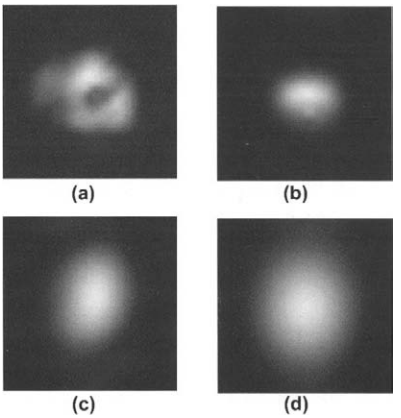

Fig. 23. Experimental intensity distributions that emerge from an Nd:YAG laser with SPEs that operated with the $TEM_{0,+1}$ mode and without SPEs that operated with the fundamental TEM_{00} mode: (a) $TEM_{0,+1}$ near field; (b) TEM_{00} near field; (c) $TEM_{0,+1}$ far field; and (d) TEM_{00} far field. (From Oron, Danziger, Davidson, Friesem and Hasman [1999b].)

SPEs were formed for $N = 1$, on fused silica substrates in a single-stage etching process using a gray-scale mask, and AR coated for $\lambda = 1.06\,\mu m$. Here again, an internal aperture was varied in order to achieve single-mode operation. The experimental results with the Nd:YAG laser are shown in fig. 23. Figure 23a presents the laser output near-field intensity distribution, corresponding to the $TEM_{0,+1}$ mode, with the expected doughnut-shaped distribution. Figure 23b depicts the near-field intensity distribution, corresponding to the fundamental TEM_{00} mode pattern (with no SPEs). Figure 23c depicts the corresponding far-field intensity distribution, where the single main lobe is evident, again indicating that all parts of the near-field pattern are in phase. Figure 23d depicts the far-field pattern from a laser operating with the fundamental TEM_{00} mode, whose cross-section area is, as expected, similar to that from a laser operating with the higher-order $TEM_{0,+1}$ mode. As evident, there is some asymmetry in the

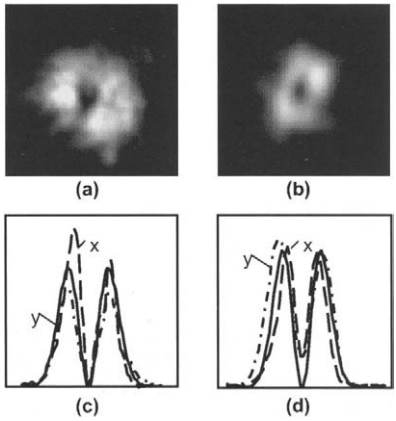

Fig. 24. Near- and far-field intensity distributions of a helical beam: (a) experimental near field; (b) experimental far field; (c) calculated and experimental near-field cross sections; dashed lines, experimental results for the x and y axes; solid lines, calculated results; (d) calculated and experimental far-field cross sections. (From Oron, Davidson, Friesem and Hasman [2000b].)

intensity distributions, which is attributed to the nonuniformity of the SPEs. An output power of 5.2 W was obtained when the laser operated with the $TEM_{0,+1}$ mode, which was higher by up to 50% with respect to that obtained from the same laser operating with the TEM_{00} mode and no SPEs.

The resonator configuration shown in fig. 19c was experimentally tested with a linearly polarized discharge-pumped CO_2 laser, operating with a single longitudinal mode. The reflective SPE was fabricated on a silicon substrate in a multistage etching process, to form 32 phase levels with a combined depth of λ, which corresponds to $N = 1$. The depth accuracy in the fabrication process was less than 3% and the RMS surface quality was better than 20 nm. Its reflectivity was better than 98%, adequate to serve as a laser reflector mirror. The diameter of the laser tube was 11 mm, and the length of the laser was 65 cm. The intra-cavity cylindrical lens ($f = 12.5$ cm) was focused on the concave ($r = 3$ m) output coupler, while an identical lens was positioned outside the cavity to collimate the output beam.

Figure 24 shows the near- and far-field intensity distributions of a helical beam that emerges from the laser after passing through the external cylindrical lens. The near-field distribution, shown in fig. 24a, had the expected doughnut shape, albeit with some distortions, due mainly to imperfections in the fabrication process of the SPE. The output power was 1.2 W. The corresponding far-field intensity distribution, shown in fig. 24b, was obtained by focusing the output beam with a spherical lens ($f = 50$ cm). Here again the beam was

doughnut shaped. The x and y cross-sections of the near- and far-field intensity distributions, compared to the calculated cross-sections derived from eq. (1), are given in figs. 24c and 24d, respectively. As evident, there was good agreement between the predicted and experimental results, including the low intensity at the center. As shown, there was some asymmetry between the x and y cross-sections of the intensity distributions, which is due to some astigmatism caused by the intra-cavity cylindrical lens. The intensity distribution at other planes maintained the same shape.

By replacing the SPE with a reflective mirror in the setup of fig. 19c and adjusting the internal aperture, the laser operated with the fundamental TEM_{00} mode, where the output power was 0.9 W. This is significantly lower than the 1.2 W obtained when the laser operated with the $TEM_{0,+1}$ helical mode.

3.5. *Self-imaging and Fourier resonators*

It is also possible to discriminate and select a single high-order mode by resorting to specialized resonator configurations. In this subsection we describe two types of resonators: resonator designs based on the Fourier transformation, and self-imaging resonators based on the Talbot effect (see Talbot [1936]). Generally, in Fourier resonators a single spatial filter is not sufficient to select a high-order mode, so two different spatial filters are used. Self-imaging resonators exploit the Talbot effect, where periodic structures, such as high-order modes, are reproduced after propagating certain distances (namely Talbot lengths).

Kermène, Saviot, Vampouille, Colombeau, Froehly and Dohnalik [1992] presented a Fourier resonator with two binary amplitude spatial filters, each placed next to a laser mirror. In this resonator, an intra-cavity focusing lens performed the Fourier transformation between the two planes where the laser mirrors were placed. The spatial filter next to the output coupler had a similar pattern to that of the desired output beam, whereas the spatial filter next to the back mirror was designed to produce the desired output beam with a uniform phase. Specifically, this back filter was designed to have high absorption in regions where the Fourier transformation of the desired intensity distribution has low intensity. For example, for a desired square intensity distribution, a square spatial filter was placed next to the output coupler and a spatial filter with absorbing lines along the zeros of a two-dimensional sinc function (which is the Fourier transformation of a square) was placed next to the back mirror. A similar design, for obtaining a uniform-phase circular intensity distribution at the laser output, was demonstrated by Saviot, Mottay, Vampouille and Colombeau

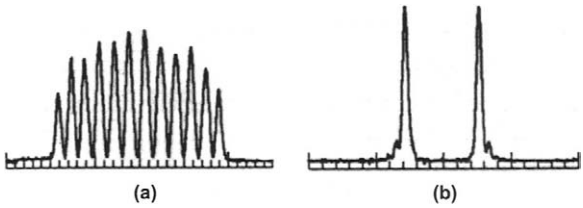

Fig. 25. Near- and far-field intensity distributions emerging from a slab waveguide CO_2 laser, operating with the 12th-order mode, with an intra-cavity wire grid. (From Morley, Yelden, Baker and Hall [1995].)

[1993]. Here the spatial filter next to the output coupler was simply a circular aperture, whereas the spatial filter next to the back mirror had concentric rings, corresponding to the zeros of the Airy pattern. Experimental results with a pulsed Nd:YAG laser, operating with such square and circular intensity distributions with output energies of 200 mJ, were obtained. Bourliaguet, Mugnier, Kermène, Barthélémy and Froehly [1999] showed that the performance of a pulsed optical parametric oscillator (OPO) could be improved by intra-cavity spatial filtering. Specifically, a five-fold increase of brightness with respect to the multimode operation was demonstrated when applying an intracavity two-dimensional wire grid designed to form a few lobes in the far field. Le Gall and Bourdet [1994] also investigated a Fourier resonator configuration in which an internal spatial filter coupled the phases of an array of CO_2 waveguide lasers. Fourier resonators were also investigated by Wolff, Messerschmidt and Fouckhardt [1999] for selecting high-order modes in broad area lasers.

Abramski, Baker, Colley and Hall [1992] exploited a one-dimensional wire grid in a slab waveguide CO_2 laser in order to select a single high-order mode. The wire grid spacing d was designed to match the periodicity of the desired mode. In principle, this by itself could lead to high modal discrimination, but in practice the alignment tolerances cannot be met, so excessive losses are introduced. The losses can be significantly reduced by resorting to a resonator with intra-cavity coherent self-imaging, based on the Talbot effect. Specifically, the resonator length L was chosen to match the Talbot length, namely, $L = \frac{1}{2}pd^2/\lambda$, where p is a small integer that corresponds to the number of imaging planes in a round-trip. Such a self-imaging Talbot effect is particularly advantageous in a waveguide laser where the boundaries reflect the light, leading to a "kaleidoscope" effect, in which a much larger periodic structure is more efficiently self-imaged. The modal properties of such a slab waveguide CO_2 laser were experimentally investigated by Morley, Yelden, Baker and Hall [1995], and their results are presented in fig. 25. It shows the near- and far-field intensity

distributions cross-sections, when the laser operated with the 12th-order mode. As evident, the 12 lobes in the near-field pattern transformed into two main lobes (of opposite phase) in the far field, indicating that the laser operates with a single mode. The wires were 75 μm thick, and output powers of up to 65 W were obtained with the single high-order mode, compared to 90 W power for the multimode operation, in a resonator length of 25.4 cm.

Self-imaging resonators based on the Talbot effect were also applied for mode selection in waveguide lasers (Banerji, Davies and Jenkins [1997]), to coherently lock arrays of diode lasers (e.g., Jansen, Yang, Ou, Botez, Wilcox and Mawst [1989]), and for phase matching the modes in waveguide CO_2 lasers with intracavity binary phase elements (Glova, Elkin, Lysikov and Napartovich [1996]). Similarly, Tang, Xin and Ochkin [1998] replaced the back mirror in a CO_2 laser with a reflective binary phase element to obtain high-output powers. In these cases, either in-phase or anti-phase operation resulted in either one high central lobe or two main lobes in the far field.

3.6. *Polarization-selective resonators*

The light emerging from most resonators is either linearly polarized or unpolarized. Linear-polarization operation is typically obtained by either inserting into the resonator a Brewster window or other polarization selective elements (such as birefringent crystals, polarizers or polarizing beam splitters), or by a polarization-sensitive pumping system (such as RF-excited slab lasers). Unpolarized light is simply obtained where there are no polarization-sensitive elements in the resonator. Also, circularly polarized light can be obtained by inserting a quarter-wave ($\lambda/4$) plate into the resonator (see for example Tröbs, Balmer and Graf [2000]). In all the above, the light polarization is uniform across the entire laser output beam. In this subsection, we present laser resonator configurations in which the polarization in different parts of the output beam can be varied, namely a laser output beam with space-variant polarization.

Space-variant polarization, such as azimuthal and radial polarizations, results in completely symmetric laser beams that can be exploited in various applications. Such polarizations have been obtained, outside the laser resonator, either by transmitting a linearly polarized laser beam through a twisted nematic liquid crystal (Stadler and Schadt [1996]) or by combining two linearly polarized laser output beams interferometrically (Tidwell, Kim and Kimura [1993]).

Azimuthal and radial polarizations have also been obtained by inserting polarization-selective elements into the laser resonator. Pohl [1972] inserted a

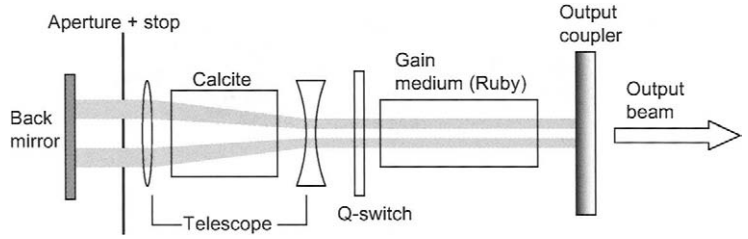

Fig. 26. Resonator configuration for selecting an azimuthally polarized mode. (From Pohl [1972].)

birefringent calcite crystal, in which the principal axis was along the z-axis (z cut), into a pulsed ruby laser in order to discriminate between azimuthal and radial polarizations. The resonator configuration is shown in fig. 26. The calcite crystal was inserted inside a two-lens telescope arrangement, so as to increase the divergence of the mode inside the crystal and thereby also the polarization discrimination. Specifically, due to different angles of refraction, the diameter of the azimuthally polarized mode differed from that of the radially polarized beam; so discrimination and selection of an azimuthally polarized mode were obtained by inserting an aperture and a stop with the appropriate diameters. Wynne [1974] generalized this method and showed experimentally, with a wavelength-tunable dye laser, that it is possible to select either the azimuthally or the radially polarized mode. This was achieved by controlling the telescope length and location, so in a certain range of telescope lengths and locations, the azimuthally polarized mode is stable whereas the radially polarized mode is unstable or vice versa.

Mushiake, Matsumura and Nakajima [1972] used a conical intra-cavity element to select a radially polarized mode. The conical element introduced low reflection losses to the radially polarized mode but high reflection losses to the azimuthally polarized mode. This method is somewhat similar to applying a Brewster window for obtaining a linear polarization. Similarly, Tovar [1998] suggested using complex Brewster-like windows, of either conical or helical shape, to select radially or azimuthally polarized modes.

Nesterov, Niziev and Yakunin [1999] replaced one of the mirrors of a high-power CO_2 laser by a sub-wavelength diffractive element. This element consisted of either concentric circles (for selecting azimuthal polarization) or straight lines through a central spot (for selecting radial polarization) to obtain different reflectivities for the azimuthal and radial polarizations. Experimentally, high output power of 1.8 kW was obtained, but the polarization purity was relatively low, with mixed transverse mode operation. Liu, Gu and Yang [1999] analyzed a

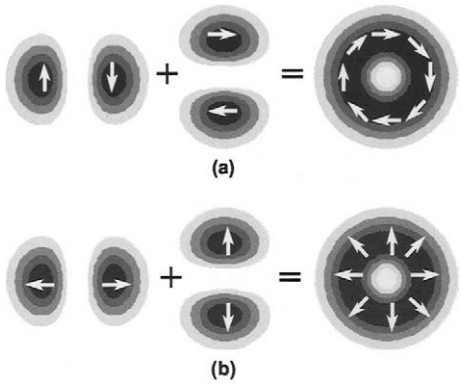

Fig. 27. Coherent superposition of two orthogonally polarized TEM_{01} modes to form azimuthally and radially polarized modes: (a) azimuthally (θ) polarized doughnut mode; (b) radially (r) polarized doughnut mode.

resonator configuration, into which two sub-wavelength diffractive elements were incorporated, to obtain a different fundamental mode pattern for two different polarizations.

Oron, Blit, Davidson, Friesem, Bomzon and Hasman [2000] presented a method for efficiently obtaining an essentially pure either azimuthally or radially polarized beam directly from a laser. It is based on the selection and coherent summation of two linearly polarized transverse modes that exist inside the laser resonator; specifically, two orthogonally polarized TEM_{01} modes. The coherent summation of $TEM_{01(x)}$ and $TEM_{01(y)}$ Laguerre–Gaussian modes (or TEM_{10} and TEM_{01} Hermite–Gaussian modes), having orthogonally linear polarizations, leads to the formation of either an azimuthally or radially polarized mode, whose vectorial field distributions have the form

$$\begin{aligned} \text{Azimuthal}: \quad & E(r,\theta) = \boldsymbol{y}E_{01(x)}(r,\theta) - \boldsymbol{x}E_{01(y)}(r,\theta) = \boldsymbol{\theta}E_0\rho^{\frac{1}{2}}\exp(-\rho/2), \\ \text{Radial}: \quad & E(r,\theta) = \boldsymbol{x}E_{01(x)}(r,\theta) + \boldsymbol{y}E_{01(y)}(r,\theta) = \boldsymbol{r}E_0\rho^{\frac{1}{2}}\exp(-\rho/2), \end{aligned} \tag{11}$$

where $\boldsymbol{\theta}$ and $\boldsymbol{r}$ are unit vectors in the azimuthal and radial directions, respectively. This coherent summation is illustrated in fig. 27. Figure 27a depicts an azimuthally polarized mode, obtained by a coherent summation of a y-polarized $TEM_{01(x)}$ mode and an x-polarized $TEM_{01(y)}$ mode, whereas fig. 27b depicts a radially polarized mode, obtained by a coherent summation of an x-polarized $TEM_{01(x)}$ mode and a y-polarized $TEM_{01(y)}$ mode.

The laser resonator configuration in which specific transverse modes are selected and coherently summed is schematically shown in fig. 28. Here, the

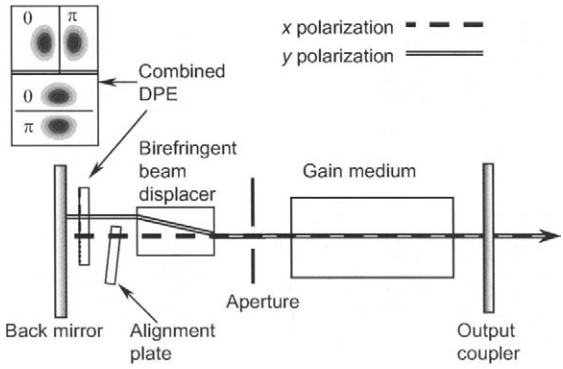

Fig. 28. Laser resonator configuration with a discontinuous phase element (DPE) for forming azimuthally or radially polarized beam. (From Oron, Blit, Davidson, Friesem, Bomzon and Hasman [2000].)

light propagating inside the laser is split and displaced by means of a birefringent beam displacer to obtain two separate paths with orthogonally polarized light. A differently oriented discontinuous phase element (DPE) is inserted in each path, adjacent to the back mirror, to select the TEM_{01} mode. Specifically, one of these modes is $TEM_{01(x)}$, and the other is $TEM_{01(y)}$. In practice, the two DPEs can be fabricated on the same substrate. In order to add the two modes coherently with the appropriate phase between them, an additional aligning plate is inserted into one of the paths (in the region after separation), so as to control the optical path by slightly tilting the window. Note that exact phase locking between the two orthogonal modes is obtained by a small coupling between them; the alignment plate brings the two modes close enough to allow this locking to occur. At the back mirror, two spatially separated TEM_{01} modes evolve, each with a different linear polarization. However, as a result of the coherent summation of these two modes, a circularly symmetric doughnut-shaped beam emerges from the output coupler.

This approach was verified experimentally with a continuous-wave lamp-pumped Nd:YAG laser into which were inserted a calcite crystal as the birefringent beam displacer, two DPEs for selecting the orthogonally polarized TEM_{01} modes, and an alignment plate to adjust the phase between the two orthogonally polarized TEM_{01} modes. The calcite crystal was 4 cm long, so the two orthogonally polarized light paths were displaced 4 mm apart. The phase elements were aligned to obtain two orthogonal TEM_{01} modes. The alignment plate was simply a flat-fused silica window with antireflection layers on both faces. To ensure that the beam emerging from the laser is indeed azimuthally or

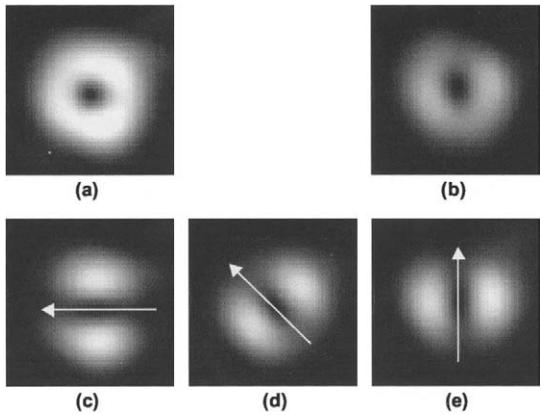

Fig. 29. Experimental intensity distributions of an azimuthally polarized beam that emerges from an Nd:YAG laser: (a) directly from the laser with no external elements; (b) after passing a horizontal $\lambda/4$ plate and a polarizer oriented at 45 degrees; (c) after passing a polarizer oriented in the horizontal direction; (d) after passing a polarizer oriented at 45 degrees; (e) after passing a polarizer oriented in the vertical direction. (From Oron, Blit, Davidson, Friesem, Bomzon and Hasman [2000].)

radially polarized, it was passed through a linear polarizer at 45 degrees. Then, the alignment plate was tilted until the intensity distribution after the polarizer had two lobes perpendicular (for azimuthally polarized) or parallel (for radially polarized) to the polarization direction. This indicated that the orthogonal TEM_{01} modes add coherently.

Some results for an azimuthally polarized beam are shown in figs. 29 and 30. Figure 29 shows the intensity distributions, detected with a CCD camera, that emerge from an Nd:YAG laser, which emits an azimuthally polarized beam. Figure 29a shows the near-field intensity distribution of the azimuthally polarized beam, emerging directly from the laser. Here the doughnut shape is evident. In order to determine the polarization of the output beam, four additional intensity distributions were detected. These are shown in figs. 29b–e. Figure 29b shows the intensity distribution of the emerging beam after passing through a quarter wave plate, whose main axis was oriented in the horizontal direction, and a polarizer oriented at 45 degrees. Here, the nearly doughnut-shaped intensity distribution (with approximately half the power) indicates that the polarization of the original beam is linear at each point. Figures 29c–e show the intensity distributions of the beam emerging from the laser, after passing a single linear polarizer oriented at different orientations. Figure 29c shows the intensity distribution with the polarizer oriented in the horizontal direction, fig. 29d that in the diagonal (45 degrees) direction and fig. 29e in the vertical direction. At these three

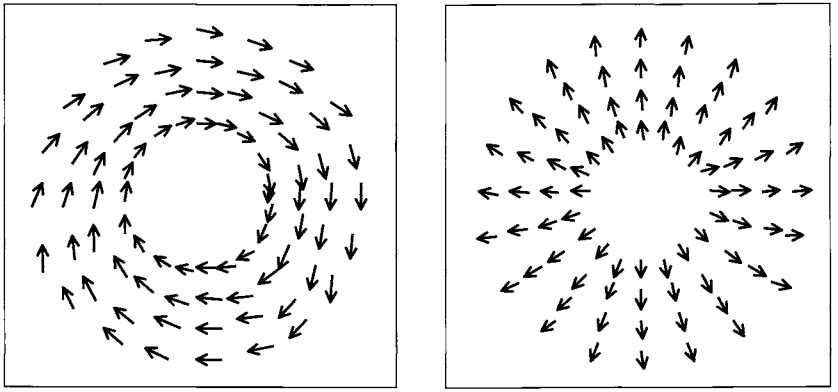

Fig. 30. Experimental plot of the space variant polarization directions of the emerging (a) azimuthally and (b) radially polarized beams. (From Oron, Blit, Davidson, Friesem, Bomzon and Hasman [2000].)

orientations, the intensity distributions have two lobes, along a line perpendicular to the polarization direction, as expected for an azimuthally polarized beam.

By measuring the intensities at each point of the distributions in figs. 29b–e, the Stokes parameters S_0–S_3 were calculated at each point of the beam, from which the polarization ellipse parameters were deduced at each point. These results, for the experimental polarization orientations for an azimuthally polarized beam, are presented in fig. 30, where the arrows indicate the direction of the main axis of the local polarization ellipse (azimuthal angle ψ), calculated by $\arctan(S_2/S_1)$. The deviation from the desired direction of polarization and the average ellipticity angle $\chi = \arcsin(S_3/S_0)$ were also calculated. The calculated deviation from the desired polarization orientation was 10 degrees, and the average ellipticity angle was found to be 8 degrees. The overall polarization purity (percentage of power that is azimuthally polarized) was determined to be 95%. As expected with a TEM_{01}-mode operation that exploits more of the laser gain medium than the fundamental Gaussian mode, the output power of our laser with azimuthal polarization was 5.2 W, that is 50% higher than with the fundamental Gaussian mode. Similar results were obtained for a radially polarized beam, as shown in fig. 30b. Note that other polarization states can be obtained by applying higher-order modes. These include high-order rotational polarization by applying TEM_{0l} modes where $l \geqslant 2$, and azimuthally or radially polarized beams having a few concentric rings with TEM_{pl} modes, where $p \geqslant 1$.

In a similar resonator configuration, it is possible to simultaneously select two different orthogonally polarized transverse modes, in order to more efficiently

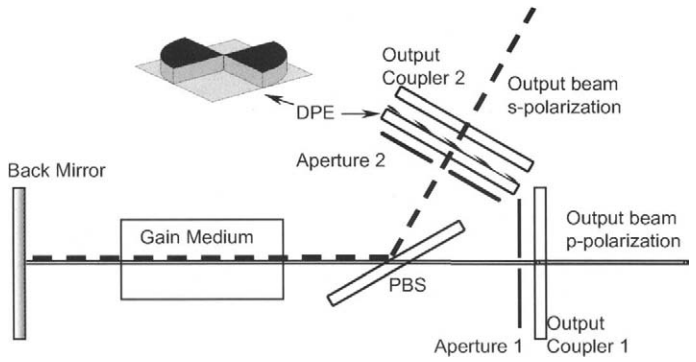

Fig. 31. Resonator configuration in order to obtain two orthogonal polarized TEM_{00} and TEM_{02} modes. (From Oron, Shimshi, Blit, Davidson, Friesem and Hasman [2001].)

exploit the gain medium. Oron, Shimshi, Blit, Davidson, Friesem and Hasman [2001] investigated laser operation with orthogonally polarized TEM_{00} and TEM_{02} modes using the configuration shown in fig. 31. The total output power with the two modes was 5.7 W, compared to 4.7 W with the single TEM_{02} mode and 3.2 W with the single TEM_{00} mode; thus, an improvement of the output power by approximately 25% over that of a laser operating with the TEM_{02} mode was obtained. Furthermore, since the two modes are orthogonally polarized, each could be manipulated separately and then combined to obtain high-output beam quality as well.

3.7. *Unstable resonators*

In this subsection, we present various mode-shaping and mode-selection techniques, which are unique to unstable resonator configurations. Several other methods involve the use of a graded-reflectivity mirror (GRM). GRMs have a continuous, nonuniform reflectivity, where typically the reflectivity is higher in the center and lower near the edges of the mirror. Generally, in a laser with a GRM output coupler, there is a dip in the center of the near-field pattern, since the reflection of the GRM is higher in the center. The analysis of GRM unstable resonators could either be based on geometrical optics, which is accurate only in a certain range of resonator parameters (see for example Bowers [1992]), or be based on diffraction analysis, which is more general (see for example Morin [1997]). Other mode-shaping and mode-selection techniques involve either the exploitation of intra-cavity apertures with various shapes, or replacing the back mirror by a mirror with a phase step.

Several methods were suggested for shaping the internal modes to obtain a specified laser output profile. Bélanger and Paré [1994] replaced the output coupler by a GRM in order to obtain a certain output beam profile with lower diffraction than with a conventional mirror. The method usually results in some decrease in the output power. Massudi and Piché [1997] showed theoretically that nearly flat-top output beams could be obtained by inserting an aperture into certain negative-branch unstable resonators. In practice however, such output beams are difficult to realize, because of the existence of a focal spot in the negative-branch resonators. Makki and Leger [2001] controlled the profile of the output beam from an unstable resonator by replacing the output coupler with a GRM and replacing the back mirror with a reflecting phase element. The phase element allowed additional shaping of the intra-cavity mode pattern so as to eliminate the dip in the center of the output beam. By proper design of the phase element, a nearly flat-top output beam was obtained.

Piché and Cantin [1991] demonstrated that by introducing a nearly π phase step in the center of a mirror, one can significantly lower the round-trip losses of the unstable resonator. This is attributed to focusing of the laser mode near the optical axis, caused by the phase step, so the output coupler reflects a larger portion of the beam. Calculations based on the Prony method were supported by experimental results with a CO_2 laser. Specifically, lasers with a phase step can operate with higher magnification than without a phase step.

Van Eijkelenborg, Lindberg, Thijssen and Woerdman [1998] isolated higher-order modes by inserting a strip aperture, a square aperture or a circular aperture into the unstable laser resonator. The mode selection was performed indirectly, by controlling the longitudinal mode of a HeXe laser, operating in the infrared ($\lambda = 3.51\,\mu m$). Different high-order modes were obtained for each aperture shape, in good agreement with calculated predictions. McDonald, Karman, New and Woerdman [2000] calculated the shapes of high-order modes in unstable resonators in which differently shaped two-dimensional apertures were inserted. They found that the high-order modes have kaleidoscope-like patterns.

3.8. *Alternative methods*

In this subsection, we present mode-selection and mode-shaping techniques, based on inserting into the resonator either specialized mirrors or specialized prisms, or elements that replace the commonly used hard-edged (binary) aperture. Rioux, Bélanger and Cormier [1977] replaced one of the laser mirrors

by a conical (axicon) mirror, to obtain high-order annular modes. In this case, either single-mode or multimode operation was obtained, depending on the resonator length and intra-cavity aperture diameter. Uehara and Kikuchi [1989] exploited an annular back mirror in order to obtain nearly Bessel–Gaussian output beams. The experimental intensity distributions were measured in good agreement with expected calculated results.

Abramochkin, Losevsky and Volostnikov [1997] obtained different spiral-type output beams from a ring laser resonator in which an intra-cavity prism that rotated the internal beam was inserted. The output beams resulted from unusual combinations of Laguerre–Gaussian beams, and they generally contained a few azimuthal lobes and exhibited rotational symmetry. Zhou, Fu, Lu, Li and Yu [1991] replaced the intra-cavity aperture by a capillary tube, and showed both theoretically and experimentally, that increased modal discrimination between the fundamental and high-order modes is obtained. Ait-Ameur [1993] proposed to replace the hard-edged aperture by a super-Gaussian aperture. Calculations revealed that with a super-Gaussian aperture of order 5 to 10, both high transverse-mode discrimination and low fundamental-mode losses could be obtained. Tovar and Casperson [1998] considered an apodized aperture with a specified amplitude transmission, in order to obtain a laser operating with hyperbolic sine Gaussian modes.

3.9. *Fabrication of intra-cavity elements*

In general, great care must be taken when fabricating elements that are inserted into the laser resonator, because any losses are greatly magnified. This is particularly true for mode-selecting and mode-shaping elements, whose light efficiency must be very high. Thus, various specialized techniques have been developed for fabricating these intra-cavity elements. These involve advanced electron beam recording, photolithographic and etching thin film deposition, and diamond turning technologies. The fabrication of some representative intra-cavity elements will be briefly described.

Binary diffractive or phase elements are generally fabricated with a one-stage etching process, using a single binary mask that is generally recorded with an electron beam, whose information is transferred to photo-resist layers with conventional photolithographic technologies. Continuous diffractive or phase elements (such as spiral phase elements) are fabricated with a more complex, multistage, etching process (see for example Hasman, Davidson and Friesem [1991]). In this fabrication method, a number N_m of binary masks are first individually recorded, and their information is transferred to photo-resist layers

that are individually etched to form the nearly continuous phase element with 2^{N_m} phase levels. Generally, when using such elements outside the resonator (for example, for beam shaping), a high efficiency of 98.6% is obtained for an element with 16 levels ($N_m = 4$). For an intra-cavity element one might typically need even higher-level resolution due to two main factors. First, an intra-cavity element is often placed next to a mirror or replaces it, so light passes through it twice in a short distance, requiring twice the level depth resolution. Second, losses are magnified inside the laser resonator, so higher efficiencies, and thereby lower losses, are required from the element. Thus, a larger number of masks N_m may be required. This implies that the multistage process has a basic drawback in fabrication complexity.

Alternatively, a one-stage etching process with a gray-scale mask can be exploited. Suleski and O'Shea [1995] recorded such a gray-scale mask on low-contrast films using visible illuminators and photo-reduction techniques. For their final blazed grating, diffraction efficiencies up to 85% were measured. Daschner, Stein, Long, Wu and Lee [1996] recorded the gray-scale mask on a specially designed high-energy beam sensitive glass, using a computer-controlled high-energy electron beam. Borek and Brown [1999] also exploited a one-stage etching process, with a gray-scale mask. Such one-stage etching processes lead to elements with a desirable continuous depth profile. However, the process requires very exact calibration procedures.

Bourderionnet, Huot, Brignon and Huignard [2000] showed that holographic optical elements can also serve as intra-cavity elements. The holographic elements were recorded in a thick photo-polymer material, using a computer-controlled spatial light modulator to control the phase of the signal beam. The holographic elements were designed to obtain a super-Gaussian output from an Nd:YAG laser ($\lambda = 1.06\,\mu m$). Unfortunately, highest diffraction efficiency of the holographic element was only 95%, which resulted in a laser output power approximately 40% lower than that from a laser with no holographic elements.

Thin-film technology could also be used to form a binary phase element (see for example Kol'chenko, Nikitenko and Troitskii [1980] or Piché and Cantin [1991]). Here, instead of etching into the substrate, a relatively thick layer is deposited on the substrate through a mask with the desired shape, which results in a binary phase element. Some elements are fabricated with a diamond-turning technique. This technique is generally exploited for forming aspherical mirrors or phase elements, such as conical elements of GPMs (see for example Van Neste, Paré, Lachance and Bélanger [1994]), where there is a circular symmetry. Due to the relatively low attainable resolution, this method is mostly used for longer wavelengths, namely, CO_2 lasers.

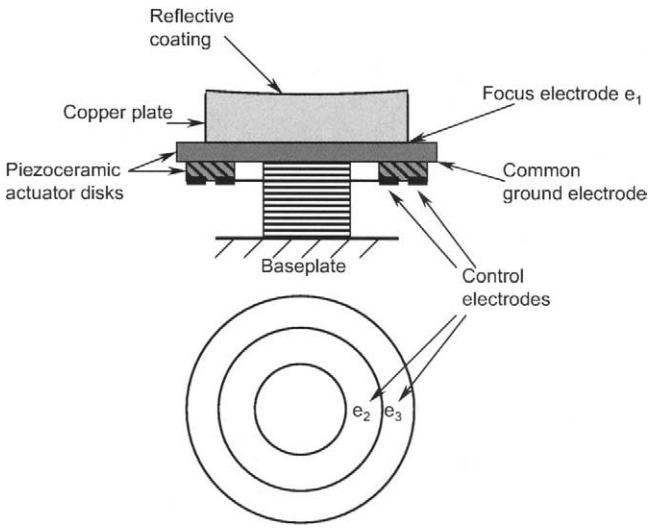

Fig. 32. Adaptive mirror. The phase profile is controlled by the three electrodes e1–e3. (From Cherezova, Chesnokov, Kaptsov and Kudryashov [1998a].)

Cherezova, Chesnokov, Kaptsov and Kudryashov [1998a,b] showed that it is possible to replace the fixed back mirror of a laser resonator with an adaptive mirror. An adaptive mirror fabricated with three electrodes can control piezoceramic actuators to form a radially symmetric phase pattern. The shape of the adaptive mirror can be electrically controlled both to obtain a predetermined shape and to correct possible aberrations in the resonator. A schematic diagram of the adaptive mirror is shown in fig. 32. This mirror was applied as a GPM in order to select super-Gaussian output beams of various orders or a doughnut-shaped output beam.

Finally, most if not all intra-cavity elements require high-quality reflective or antireflective coatings in order to minimize losses. Also, high surface quality (low roughness) is required to reduce scattering losses, and high parallelism is required from transmittive elements in order to maintain the optical path after insertion.

§ 4. Properties of the laser output beams

In this section, we consider certain properties of the laser output beams. These include beam quality, output power and field distributions. Several specific laser output beams are presented.

4.1. *Beam quality*

There are various criteria for evaluating the quality of laser output beams. Such criteria are not universal, but depend on the specific application. The most widely used criteria for beam quality are based on focusability, or a product of beam width and beam divergence. However, there are different definitions of width and divergence. Other criteria are based on phase space analysis, on coherence, or on thermodynamic limits (entropy). Here, several beam quality criteria are considered.

4.1.1. Second-order moments (M^2)

The quality of the beam emerging from a laser is most commonly defined by its focusability, determined by the product of beam waist and beam divergence. The measure for the beam quality is the second-order moment beam propagation factor introduced by Siegman [1990], namely, the M^2 value, given by the ratio between the space–bandwidth products of the beam and that of a Gaussian beam, as

$$M^2 = \frac{w\theta}{w_{\text{Gaussian}}\theta_{\text{Gaussian}}}, \tag{12}$$

where $w = (\langle w^2 \rangle)^{\frac{1}{2}}$ and $\theta = (\langle \theta^2 \rangle)^{\frac{1}{2}}$. Consequently, the optimal beam has a Gaussian shape, with a minimal waist–divergence product, which is limited only by diffraction. Such an optimal beam, with $M^2 = 1$, can be obtained from a laser operating with a single fundamental TEM_{00} mode. Modifications of the beam-quality criteria are based on different definitions of w and θ, namely, the angle or waist in which a certain percentage of the energy is contained. These criteria agree with the M^2 value for Gaussian beams. However, for other types of beams, such as high-order modes or nearly flat-top beams, the criteria may deviate significantly.

For any beam, the M^2 value is left unchanged by propagation of the beam or by simple optical elements such as spherical mirrors and lenses, a combination of those, or any optical system that can be represented by an ABCD matrix (see Yariv [1991] for details). Moreover, Siegman [1993] showed that binary (π) phase plates cannot improve the M^2 value. Later, Zhao [1999] also showed that other step-phase plates cannot improve the M^2 value. Also, aberrations in an optical system may be related to the deterioration of the M^2 value for a beam passing through it.

M^2 values for various types of beams have been calculated (see for example Siegman [1990] or Saghafi and Sheppard [1998]). Specifically, for a beam

derived from a laser operating with the Hermite–Gaussian modes, the M^2 value is given by $1+n+m$, while a beam derived from a laser operating with the Laguerre–Gaussian modes has $1+2p+|l|$. For a multimode laser, the M^2 value is mostly determined by that of the highest-order mode, although the total number of modes, $N_T = \frac{1}{2}M^2(M^2+1)$, could be very large. So, the mode content of a laser cannot generally be determined from the M^2 value. Another disadvantage of this criterion is that certain types of beams that are desired for various applications, such as a flat-top beam, have very high M^2 values.

For beams whose field distribution cross-section differs between the x and y axes, it is useful to define a more general value, namely $M^4 = M_x^2 \cdot M_y^2$. A similar definition could be applied for radially symmetric beams. M^4 values have been calculated for beams derived from lasers operating with the Hermite–Gaussian and the Laguerre–Gaussian modes, yielding $M^4 = (1+2m)(1+2n)$ and $M^4 = (1+2p+|l|)^2 - l^2$, respectively (see Murphy [1999]).

4.1.2. Wigner distribution function (WDF)

The Wigner distribution function (WDF) was introduced by Wigner [1932] and has been applied in many branches of physics and optics (see Dragoman [1997]). One of these applications relates to beam quality. The WDF of a beam is given by

$$W(\boldsymbol{r}, \boldsymbol{p}) = \lambda^{-2} \int \mathrm{d}^2\Delta\boldsymbol{r} \exp(-2\pi \mathrm{i}\boldsymbol{p}\Delta\boldsymbol{r}/\lambda)\, \psi(\boldsymbol{r} + \tfrac{1}{2}\Delta\boldsymbol{r})\, \psi^*(\boldsymbol{r} - \tfrac{1}{2}\Delta\boldsymbol{r}), \tag{13}$$

where $\boldsymbol{r} = (x, y)$ is the spatial coordinate, $\boldsymbol{p} = (p_x, p_y)$ is the frequency coordinate, and ψ denotes the field distribution.

Gase [1995] provided a WDF representation of Laguerre–Gaussian modes. Simon and Agarwal [2000] simplified this representation, and obtained simple relations between the WDF of Laguerre–Gaussian modes and the WDF of Hermite–Gaussian modes. The WDF of Laguerre–Gaussian modes is

$$W_{p,l}(\boldsymbol{r}, \boldsymbol{p}) = (2/\lambda)(-1)^{2p+|l|} \mathrm{L}_{p+|l|}(4[Q_0 \pm Q_2])\, \mathrm{L}_p(4[Q_0 \mp Q_2]) \exp(-4Q_0), \tag{14}$$

where $Q_0 = \frac{1}{2}(\boldsymbol{r}^2/w^2 + \pi^2 w^2 \boldsymbol{p}^2/\lambda^2)$, $Q_2 = \pi\lambda^{-1}(xp_y - yp_x)$, and L_p are the Laguerre polynomials of order p. For the TEM_{00} fundamental mode, a four-dimensional Gaussian is obtained. For all other modes, a more complicated function, but with a larger Gaussian envelope, is obtained.

A method to establish the WDF of a beam experimentally was suggested by Hodgson, Haase, Kostka and Weber [1992]. Various beam-quality parameters

can be obtained from the WDF. Specifically, either the M^2 or the M^4 values can be derived from the second-order moments of the WDF (see Dragoman [1997]), which corresponds to the four-dimensional volume surrounded by the envelope of the WDF (or to the phase-space area, given by Murphy [1999]). Also, the total coherence function K was derived by Eppich, Johansson, Laabs and Weber [2000], as

$$K = \lambda \int W(\boldsymbol{r}, \boldsymbol{p})^2 \, \mathrm{d}\boldsymbol{r} \, \mathrm{d}\boldsymbol{p} = \lambda \, \mathrm{Tr}(WW^{\dagger}), \tag{15}$$

which is maximal for a coherent (or a single-mode) beam.

The total coherence function of eq. (15) is inversely proportional to the actual (net) volume of the WDF. This volume may be only a part of the envelope volume. For lasers operating with the fundamental Gaussian mode or multimodes, the actual and envelope volumes coincide, whereby the envelope is completely full. Moreover, for lasers operating with any single high-order mode, the total coherence function K is unity, just as for a laser operating with the fundamental Gaussian mode. This implies that the actual volume of the WDF is minimal. For lasers operating with a few modes (each of equal power), the actual volume of the WDF is the number of modes.

4.1.3. Coherence and entropy

Wolf and Agarwal [1984] exploited coherence theory (see for example Born and Wolf [1965]) to show that if there is no degeneracy, each mode is completely spatially coherent. Moreover, complete spatial coherence can occur only in a laser operating with a single mode (or in some combinations of degenerate modes) and cannot occur in a multimode laser. Visser, Friberg and Wolf [2001] introduced the phase-space product, which can be exploited to obtain a measure of the beam quality for partially coherent beams. This product expresses the effective coherence area of the source multiplied by the effective angular spread of the beam, and coincides with the M^2 value for fully coherent beams. A minimal value of unity was obtained for a class of laser beams, which also included the lowest-order Gaussian mode.

Another approach, which differentiates between single-mode and multimode laser operation, was introduced by Graf and Balmer [1996]. The analysis of the beam quality is based on the second law of thermodynamics, namely, on entropy. In order to study the limits of beam shaping, the entropy of a laser operating with various transverse modes was calculated to yield

$$S_1 \approx \sum_{\text{mode}} \tfrac{1}{2} \ln(n_{\text{mode}}) \quad \text{for} \quad n_{\text{mode}} \gg 1, \tag{16}$$

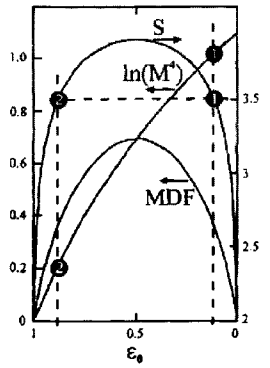

Fig. 33. Calculation of entropy, MDF and $\ln(M^4)$, for a superposition of the two lowest-order modes, as a function of the portion of the lowest-order mode ϵ_0. The entropy was calculated for a total number of 100 photons. (From Graf and Balmer [1996].)

where n_{mode} is the number of photons in the resonator mode. For a constant number of photons $n_{\text{tot}} = \sum_{\text{mode}} n_{\text{mode}}$, the maximal entropy is obtained when the photons are equally distributed among all the modes, whereas the minimal entropy is obtained when the laser operates with a single mode. Moreover, the second law of thermodynamics ($\mathrm{d}S \geqslant 0$) implies that photons can only be transferred from mode 1 to mode 2 if $n_1 \geqslant n_2$, so a transformation from multimode operation to single-mode operation is not possible. Also, the entropy of a single high-order mode is equal to that of a single Gaussian mode. Thus, it is possible thermodynamically to transform a high-order mode into a Gaussian beam without losses.

The entropy in eq. (16) depends on the total number of photons. Similarly, it is possible to define the mode distribution function (MDF) that does not depend on the number of photons. This MDF was referred to as the information entropy by Bastiaans [1986], namely

$$\text{MDF} = -\sum_{\text{mode}} \varepsilon_{\text{mode}} \ln \varepsilon_{\text{mode}}, \quad \varepsilon_{\text{mode}} = \frac{n_{\text{mode}}}{n_{\text{tot}}}. \tag{17}$$

The entropy and MDF were compared to the M^4 value for a laser operating with the two lowest-order modes. The results, as a function of the relative number of photons in each mode, are presented in fig. 33. Here, both the entropy and the MDF reach a maximum (poorest beam quality) when the photons are equally divided between the two modes, namely $\varepsilon_0 = \varepsilon_1 = \frac{1}{2}$, whereas the M^4 value decreases monotonically with ε_0. Thermodynamically, it is possible to reduce the M^4 value from that shown by point **1** to that shown by point **2** since the entropy of these two states is the same.

It should be noted that the coherence properties, the MDF and the entropy depend significantly on the modal structure of the beam. This modal structure can be evaluated from intensity distribution cross-section measurements (see for example Cutolo, Isernia, Izzo, Pierri and Zeni [1995] or Santarsiero, Gori, Borghi and Guattari [1999]) or coherence measurements (Warnky, Anderson and Klein [2000]). Thus, the MDF and entropy can be measured experimentally. Also, the entropy is related to the possible brightness improvement of a beam. The brightness is inversely proportional to the M^4 value, thus, a brightness improvement is concomitantly obtained with the reduction of the M^4 value. Note that there are two possible orthogonal polarization states, and the above discussion is valid for each of them.

4.2. *Intensity and phase distributions*

In this subsection, we consider the field distributions of beams that emerge from laser resonators. Properties of such field distributions along with methods to distinguish between them are presented. Moreover, methods to improve the focusability of beams having specified field distributions are demonstrated both theoretically and experimentally.

4.2.1. Uniform phase distribution

Beams with a uniform phase distribution can be shaped or transformed using various techniques (see for example Bryngdahl [1974] and Davidson, Friesem and Hasman [1992]). The most widespread laser output beam with uniform phase is the Gaussian beam, in which the transverse intensity distribution is maintained while propagating, leading to simple propagation properties. Such Gaussian beams can be readily obtained from lasers operating with only the fundamental TEM_{00} mode. For other beams with uniform phase, the transverse intensity distribution is changed during propagation, and their M^2 value is greater than unity. Their propagation properties depend on their intensity distributions in the near field. For example, the propagation properties of super-Gaussian beams, which can be obtained from laser resonators with intra-cavity diffractive elements or GPMs, were analyzed by Parent, Morin and Lavigne [1992].

4.2.2. Binary phase distribution

Beams emerging from a laser operating with a high-order Hermite–Gaussian mode or a high-order degenerate (non-helical) Laguerre–Gaussian mode have

binary phase distributions, which consist of lobes and rings, where neighboring lobes or rings have opposite phases (π phase shift). Casperson [1976] compensated for the phase differences between neighboring lobes or rings, by letting the output beam pass through a binary phase element with π phase shifts in proper locations. This increased the peak intensity and power in the main lobe of the far-field intensity distribution, implying a better beam quality. Yet, Siegman [1993] calculated that the beam quality, in terms of M^2 is not improved but remains the same. Indeed, he concluded that binary phase plates cannot improve the M^2 value. The contradiction between the two approaches results from different criteria for beam quality. The beam quality in accordance to percentage of power in the main lobe criterion is hardly affected by low-power side-lobes, whereas in accordance to the M^2 criterion the side-lobes contribute significantly to the improvement in the M^2 value.

Optimized binary phase-compensating elements were tested experimentally by Casperson [1977] and Casperson, Kincheloe and Stafsudd [1977] with HeNe and CO_2 lasers, yielding improvement in the peak power and percentage of power in the main lobe, in agreement with predictions. Lescroart and Bourdet [1995] analyzed binary phase-compensating elements for improving the far-field characteristics of an array of waveguide lasers and determined the trade-off between a main lobe with high peak but with side-lobes to that of main lobes of lower power concomitant with very low side-lobes. Lapucci and Ciofini [1999] optimized the design of a binary phase-compensating element for narrow annular laser sources. Note that, in a laser configuration in which a DPE is inserted next to the output coupler, as shown in fig. 12 (see sect. 3.3), there is no need for a phase-compensating element, since the mode-selecting DPE acts also as a phase-compensating element.

Baker, Hall, Hornby, Morley, Taghizadeh and Yelden [1996] showed that by introducing a binary phase-compensating element, the beam emerging from a waveguide laser operating with a high-order antisymmetric mode is transformed so that the far-field distribution consists of a high-intensity main lobe and low-intensity side-lobes. Moreover, by resorting to spatial filtering in the far-field, the side-lobes were eliminated, thereby significantly improving the M^2 value with a relatively small decrease in power. Specifically, an original beam with $M_x^2 = 21.7$ was transformed into a beam with M_x^2 close to unity with an efficiency of 59%.

4.2.3. Helical phase distribution

In general, the intensity distribution of a helical laser beam is the same as that of a doughnut-shaped laser beam, but their field distributions are distinctly different.

Fig. 34. Experimental interference fringe patterns: (a) Gaussian beam; (b) lowest-order helical beam; (c) lowest-order helical beam of opposite helicity. (From Harris, Hill, Tapster and Vaughan [1994].)

Specifically, the doughnut-shaped laser beams are composed of an incoherent superposition of two TEM_{0l} modes. For example, when the two field distributions of the $TEM_{01(x)}$ and $TEM_{01(y)}$ modes in eq. (6) are added incoherently, they form a hybrid mode whose intensity distribution is doughnut-shaped. On the other hand, when they are added coherently with the appropriate phase, they form a pure helical mode.

Several techniques were developed to distinguish between helical and doughnut beams, and between helical beams of opposite helicity. In one technique, the determination whether a beam is helical, having a phase of $\exp(i\theta)$, is done by examining the interference of the beam with its mirror image or with a reference beam (see Indebetouw [1993], Harris, Hill and Vaughan [1994], or Harris, Hill, Tapster and Vaughan [1994]). Examples of such interference patterns are shown in fig. 34. As evident, the helicity can be easily obtained from the fringe pattern.

Alternatively, one can let the emerging beam pass through another SPE. An SPE having a phase of $\exp(-il\theta)$ will focus the helical beam to obtain a main lobe with a high central peak intensity, whereas one having a phase of $\exp(+il\theta)$ will diverge it further away from the center. This property is unique to the helical beams formed by the $TEM_{0,+l}$ modes. For the beams formed by the hybrid mode, either one of these two SPEs will focus the hybrid beam to a main lobe with a high central peak intensity, since all parts of the beam are approximately in phase. Experimental results for the helical beams formed by the $TEM_{0,+1}$ mode are shown in fig. 35, along with those predicted for hybrid and helical beams. Figure 35a shows the cross-sections of the far-field intensity distributions with the first phase-correcting SPE having a phase of $\exp(-i\theta)$. As evident, there is a main lobe with a high central peak intensity and very low side-lobes, in agreement with those predicted for a helical beam, while the incoherent hybrid beam has more power spreading. Figure 35b shows the corresponding far-field cross-sections of the intensity distributions with the second SPE of $\exp(i\theta)$. Here the energy spreads out from the center to form an annular shape, as expected for a helical beam. However, for a hybrid beam, no spreading should occur, and there

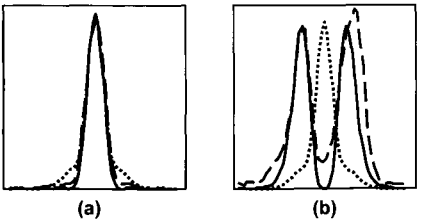

Fig. 35. Experimental and calculated far-field intensity distribution cross sections with an additional transmittive SPE: (a) SPE of exp(−iθ); (b) SPE of exp(+iθ) (dashed lines, experimental results; solid lines, calculated results for the coherent–helical; dotted lines, calculated results for the incoherent–hybrid). (From Oron, Davidson, Friesem and Hasman [2000b].)

still is one main central lobe. These results clearly indicate that the emerging beam is indeed helical.

An interesting property of helical beams is that their M^2 value can be significantly improved. Oron, Davidson, Friesem and Hasman [2000a] showed that continuous-spiral phase elements can improve the M^2 value of helical beams. Specifically, a single high-order helical beam was transformed into a nearly Gaussian beam. An arrangement for transforming the helical output beam into a nearly Gaussian beam is shown schematically in fig. 36. A helical $\mathrm{TEM}_{0,+l}$ beam, with a field distribution given by eq. (1), emerges from the laser in which a reflective SPE is inserted. The beam is collimated by a cylindrical lens, and its M^2 value is $1+l$. In the optical mode converter, the collimated beam first passes through a transmissive SPE, which introduces a phase of exp(−i$l\theta$), thereby modifying the helical-phase distribution into a uniform distribution yielding $E_0\rho^{|l|/2}\mathrm{L}_p^{|l|}(\rho)\exp(-\rho/2)$.

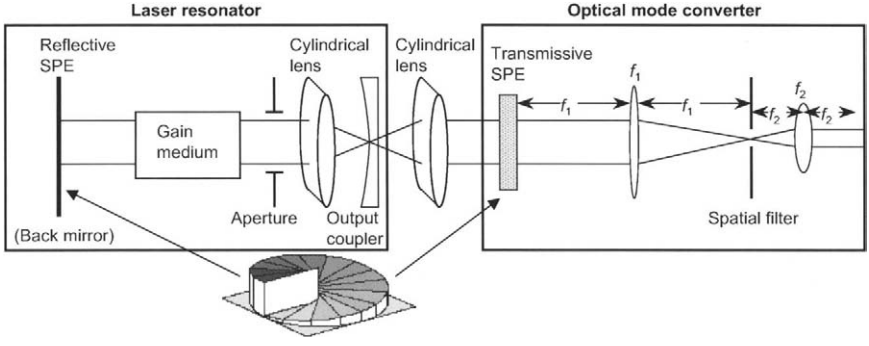

Fig. 36. Basic configuration of a laser resonator that yields a high-order helical mode and an optical mode converter that yields a nearly Gaussian mode. (From Oron, Davidson, Friesem and Hasman [2000a].)

Table 1
Initial and final M^2 values and transformation efficiency η, for a laser operating with either the fundamental mode or high-order helical modes

Mode	Initial M^2	Final M^2	Transformation efficiency η
TEM_{00}	1	1	100%
$TEM_{0,+1}$	2	1.036	94%
$TEM_{0,+2}$	3	1.06	87%
$TEM_{0,+3}$	4	1.07	80%
$TEM_{0,+4}$	5	1.07	74%

Analysis based on Fourier transformation of the near field and the second-order moments reveal that the phase modification with the external SPE reduces the M^2 value significantly, from $1+l$ to $(1+l)^{1/2}$. This result is in contrast with that obtained for a laser operating with degenerate modes, where a correcting binary-phase plate can improve the peak power of the far-field intensity distribution, but not the M^2 value. Moreover, the phase modification significantly changes the far-field intensity distribution, yielding a high central lobe and low ring-shaped side-lobes that contain only a small portion of the total power (e.g., 6% for a laser operating with the $TEM_{0,\pm1}$ modes). Thus, by exploiting a simple spatial filter (e.g., a circular aperture), it is possible to obtain a further significant improvement in the M^2 value. Specifically, a nearly Gaussian beam, with M^2 near 1 (theoretically 1.036 for the $TEM_{0,+1}$ mode), with only a small decrease in output power is obtained. Table 1 shows the calculated initial and final (after spatial filtering) M^2 values, as well as the transformation efficiency η, denoting the percentage of power in the main lobe, for a laser operating with either the fundamental mode or in high-order helical modes. Note that the transformation efficiency decreases as the order of the mode increases.

The configuration shown in fig. 36 was tested with a linearly polarized CO_2 laser in which a reflective SPE replaced the usual back mirror. The SPE was designed to ensure that the laser operated with the helical $TEM_{0,+1}$ mode, as described in sect. 3.4. The optical mode converter contained a transmissive SPE formed on zinc selenide substrate, a telescope configuration of two lenses – the first ($f_1 = 50$ cm) placed 50 cm from the SPE and the second ($f_2 = 25$ cm) 75 cm from the first – and a spatial filter in the form of a circular aperture.

The intensity distributions were detected at the spatial filter plane and the output plane with a pyroelectric camera. The results are presented in figs. 37 and 38. Figure 37 shows the detected intensity distributions, along

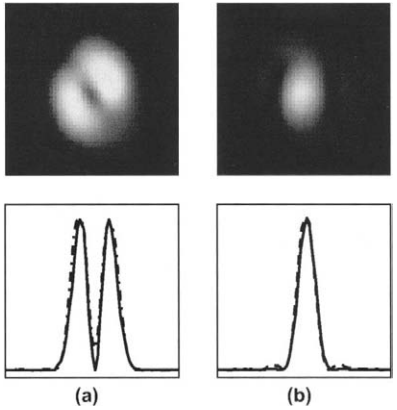

Fig. 37. Detected intensity distributions and experimental and calculated intensity cross sections at the spatial-filter plane: (a) without SPEs; and (b) with a transmissive SPE. (Solid lines, calculated; dashed lines, experimental). (From Oron, Davidson, Friesem and Hasman [2000a].)

with calculated and experimental intensity cross-sections at the spatial filter plane. Figure 37a shows the intensity distribution and cross-sections without the transmissive SPE. Thus, the usual nearly doughnut-shaped distribution of a helical beam whose phase was not compensated by the transmissive SPE is obtained. Figure 37b shows the intensity distribution and cross-sections when the transmissive SPE was inserted. As is evident, there is a high central peak with low side-lobes that are removed by spatial filtering, yielding a nearly Gaussian beam. Moreover, the detected intensity distribution is narrower than that obtained with no SPE, indicating the improvement of M^2.

Figure 38 shows photographs of the detected intensity distributions along with calculated and experimental intensity cross-sections at the output of the optical mode converter. Here, the calculated results were obtained by Fourier transformation of the field distribution in the spatial filter plane. Figure 38a shows the intensity distribution and cross-sections at the output plane, when the mode converter includes the SPE but no spatial filter. This is simply an image of the doughnut-shaped helical beam from the laser, whose intensity distribution results from a $TEM_{0,+1}$ mode. The SPE in this case does not affect the intensity distribution at the output plane but only its phase. Figure 38b shows the detected intensity distribution and cross-sections at the output plane with both the SPE and the spatial filter in the mode converter. As predicted, the intensity distribution has a Gaussian shape. In this case the efficiency η was 85%, which is somewhat lower than the calculated limit of 94%. The M^2 value of this beam was measured to be better than 1.1, as expected.

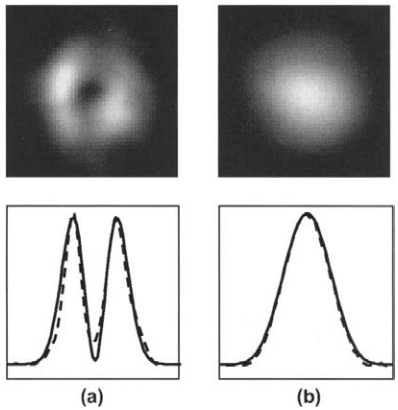

Fig. 38. Detected intensity distributions and calculated and experimental intensity cross sections at the output of the optical mode converter: (a) without a spatial filter; and (b) with a spatial filter (solid lines, calculated; dashed lines, experimental). (From Oron, Davidson, Friesem and Hasman [2000a].)

4.2.4. Several transverse modes

When the laser operates with multiple modes, i.e., fundamental and higher order modes, the emerging beam quality is relatively poor and is mainly determined by the highest-order mode. In such lasers the phase distribution of the output beam is random, and little, if anything, can be done to improve the quality of the beam. When the laser operates with a single high-order mode, the emerging beam quality is still inferior to that from a laser operating with the fundamental mode, because the intensity distribution and the divergence of the beam are relatively large. Yet, a beam which originates from a laser operating with a single high-order mode has well-defined amplitude and phase distributions, so in accordance to entropy, it is allowed thermodynamically to efficiently transform it into a nearly Gaussian beam (see sect. 4.1.3).

A laser may also operate with only a few modes, where most of the modes between the fundamental and the highest-order modes are not present. Here again the phase distribution is undefined at any point of the beam emerging from the laser. Yet, Oron, Davidson, Friesem and Hasman [2001] demonstrated that beam quality could be improved in a laser operating with a limited number of modes N, much smaller than N_T, namely,

$$N \ll N_T = \tfrac{1}{2}[M^2(M^2+1)] \approx \tfrac{1}{2}\max(1+2p+|l|)^2. \tag{18}$$

In accordance with the total coherence parameter K of eq. (15), the beam quality depends only on the number of modes and their relative powers. Thus,

according to the Wigner algebra, it is possible to reduce the WDF envelope volume of a beam from a laser operating with few modes, where the condition in eq. (18) is valid, towards that of the actual volume, thereby allowing the desired transformation that will improve the quality of the laser output beam. Such an improvement will be illustrated for a laser operating with only two incoherent transverse modes $TEM_{1,\pm1}$, whose M^2 value is 4. For comparison, the number of modes in a multimode laser with the same M^2 would be 10 (see eq. 18).

An Nd:YAG laser in which an annular DPE, consisting of a single discontinuity ring with a specified radius was inserted into the resonator, as shown in fig. 12, to simultaneously select both helical $TEM_{1,\pm1}$ modes. These two selected modes have the same radial dependence, but a different azimuthal dependence; thus, even an incoherent combination of these modes can be manipulated together in the radial direction. The optical beam converter contained a telescope configuration of two lenses with a spatial filter in the form of a circular aperture. The intensity distributions next to the output coupler, at the spatial filter plane and at the output plane, were detected with a CCD camera.

Since the DPE is placed next to the output coupler, the emerging field distribution does not have the usual π phase shift between the two rings, so the far-field intensity distribution will be significantly affected. It now has a central ring, which contains most of the output power, and ring-shaped side-lobes that contain only a small portion of the power (e.g., 20.4% for a laser operating with the $TEM_{1,\pm1}$ modes). Thus, by exploiting the additional converter with a simple spatial filter (e.g., a circular aperture), it was possible to obtain a significant improvement in the M^2 value. Specifically, a nearly doughnut-shaped beam, having M^2 near 2 (theoretically 2.04 for the $TEM_{1,\pm1}$ modes), was obtained with a relatively small decrease (20.4%) in output power. Such a reduction in M^2 leads to a significant increase in the brightness of the beam, proportional to P/M^4, where P is the power, leading to an improvement by a factor of 2.9.

The WDF of the $TEM_{1,+1}$ mode has been calculated, and some representative results are shown in fig. 39. Since the Wigner distribution is four-dimensional, only a subspace which includes the origin and where $\boldsymbol{r}$ is parallel to $\boldsymbol{p}$ is presented. Figure 39a shows the WDF of a $TEM_{1,+1}$ mode, which consists of a central negative distribution, indicating a central phase singularity (vortex), and surrounding concentric rings. Figure 39b shows the WDF after passing through a DPE which eliminates the π phase shift between the two rings in the field distribution of the $TEM_{1,\pm1}$ mode. As evident, the shapes of the rings are not whole, leading to a high (and larger) central negative distribution, and more spread-out side-lobes. This is the first stage in contracting the WDF. Figure 39c shows the far-field WDF, which is obtained after Fourier transformation. This

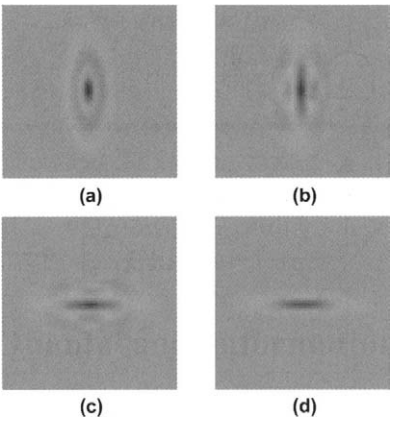

Fig. 39. Wigner distribution function of helical $TEM_{1,+1}$ mode at various locations: (a) WDF of original $TEM_{1,+1}$ mode; (b) WDF of $TEM_{1,+1}$ mode after passing an annular DPE; (c) far-field WDF of $TEM_{1,+1}$ mode after passing an annular DPE; (d) WDF of $TEM_{1,+1}$ mode after passing an annular DPE and spatial filtering. All distributions are identical to those of the $TEM_{1,-1}$ mode and to an incoherent summation of the two modes. (From Oron, Davidson, Friesem and Hasman [2001].)

Fourier transformation practically rotates the WDF by 90 degrees, to exchange the $\boldsymbol{r}$ and $\boldsymbol{p}$ axes. The last stage consists of spatial filtering, which cleans the WDF from most of the side-lobes, yielding a WDF similar to that of a $TEM_{0,+1}$ mode, still with a central negative distribution, but only a single outer ring. This WDF is shown in fig. 39d. Since the two modes $TEM_{1,+1}$ and $TEM_{1,-1}$ have similar radial dependence (though different azimuthal dependence), the above subspace of the WDF is the same for both modes, so figs. 39a–d actually show the WDF of either one of the two $TEM_{1,\pm1}$ modes or of an incoherent superposition of the two (since the WDF of an incoherent summation of two modes is the sum of the WDFs of these modes). Note that for only one of these modes is it possible to further improve the beam quality with an SPE (see sect. 4.2.3).

The experimental results are presented in figs. 40 and 41. Figure 40 shows the detected intensity distributions, along with calculated and experimental intensity cross-sections in the near and far fields respectively. Figure 40a shows the intensity distribution and cross-sections at the output from the laser. The intensity distribution shows the two rings of the $TEM_{1,\pm1}$ modes. Figure 40b shows the corresponding far-field intensity distribution and cross-sections. There is a central doughnut-shaped pattern with some low side-lobes, that are later removed by the spatial filtering, to obtain a nearly doughnut-shaped beam.

Figure 41 shows the near- and far-field intensity distributions along with

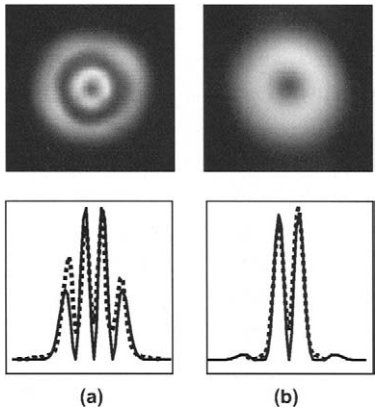

Fig. 40. Detected intensity distributions and calculated and experimental intensity cross sections at near and far fields: (a) at the output of the laser; and (b) at the spatial filter plane. (Solid lines, calculated; dashed lines, experimental). (From Oron, Davidson, Friesem and Hasman [2001].)

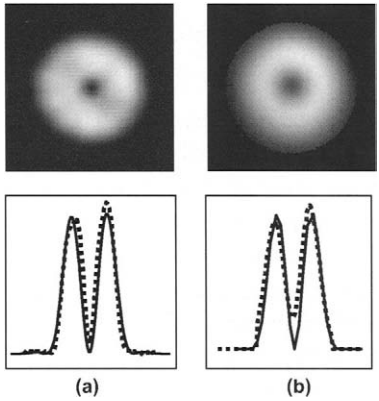

Fig. 41. Detected intensity distributions and calculated and experimental intensity cross-sections at the near and far fields after the optical mode converter: (a) near field; (b) far field. (Solid lines, calculated cross sections; dashed lines, experimental cross-sections). (From Oron, Davidson, Friesem and Hasman [2001].)

calculated and experimental intensity cross-sections of the beam at the output of the optical beam converter. As predicted, the intensity distribution is doughnut-shaped in both the near and far fields. In this case the measured efficiency was 76%, in agreement with the calculated limit of 79.6%. The M^2 value of this beam was nearly 2, as expected, leading to significant brightness improvement, in agreement with prediction.

The output power was 9.5 W directly from the laser, and 7.2 W after the mode converter. For a similar laser, with no phase element, the output power was only 5.5 W, obtained by simply opening the aperture to allow $TEM_{0,\pm1}$-mode operation; however, in this case, the laser operation included the fundamental mode, which was not suppressed. Overall, a high-quality doughnut beam was obtained, with a significantly higher power than would normally be obtained. Note, the transformation efficiency in this case was 79.6%, but it could be increased to 100% by resorting to SPEs, rather than DPEs, and selecting high-order helical modes having different p but the same l, such as $TEM_{0,+2}$ and $TEM_{1,+2}$ modes for laser operation.

4.3. *Selected applications*

In this subsection, selected applications that require special laser beam properties are briefly described, along with the possible mode-shaping or mode-selecting methods. Some applications require that the laser beam have special transverse intensity distributions, such as doughnut shape, which are particularly useful for trapping particles and atoms. Specifically, Sato, Harada and Waseda [1994] exploited doughnut-shaped beams in order to trap small metallic particles. Kuga, Torii, Shiokawa, Hirano, Shimizu and Sasada [1997] exploited doughnut-shaped Laguerre–Gaussian beams to trap laser-cooled rubidium atoms in the dark region of the beams. Doughnut-shaped beams can have additional interaction with trapped particles. He, Friese, Heckenberg and Rubinsztein-Dunlop [1995] showed that if the trapping beam is helical, the angular momentum from the laser beam is transferred to absorptive particles. One can control the angular momentum transfer by changing the helicity of the beam. Moreover, a radially polarized laser beam can be applied for accelerating electrons (Liu, Cline and He [1999]). Doughnut-shaped beams were also used by Charters, Luther-Davies and Ladouceur [1999] for directly exposing photosensitive materials to form waveguides. They showed that with doughnut-shaped beams the uniformity of the waveguide refraction index is better than with conventional beams with Gaussian profile.

Other applications require that the laser beams have special phase distribution such as a helical beam with a phase singularity. The properties of such helical beams, namely optical vortices, were analyzed by Soskin, Gorshkov, Vasnetsov, Malos and Heckenberg [1997], who developed various rules regarding the topological charge and angular momentum that characterize the propagation of such beams or combinations of such beams, and showed annihilation and

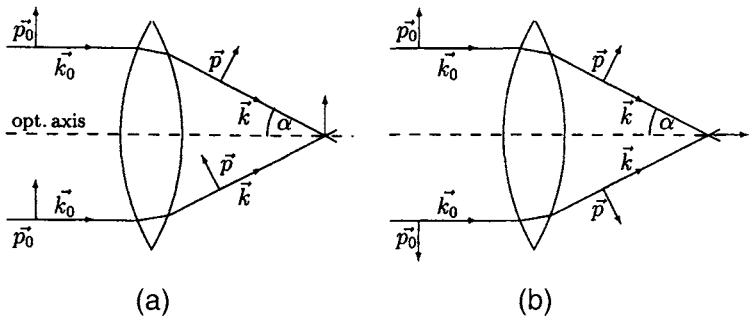

Fig. 42. Ray-tracing geometry and polarized light orientation for focusing collimated beams: (a) linearly polarized beam; and (b) radially polarized beam. (From Quabis, Dorn, Eberler, Glöckl and Leuchs [2000].)

appearance of new vortices. Courtial, Robertson, Dholakia, Allen and Padgett [1998] studied the rotational frequency shift of light beams, which is proportional to the photon angular momentum. Experimental measurements were performed with helical Laguerre–Gaussian beams and radially polarized (or other specially polarized) beams, in the millimeter wavelength range.

Still other applications require that the laser beams have special polarization properties. Specifically, Marhic and Garmire [1981] exploited azimuthally polarized CO_2 laser beams for transmission through hollow metallic waveguides. The azimuthally polarized beam has a significantly higher reflection, and consequently lower transmission losses through the hollow waveguides. In laser material processing applications, the proper choice of polarization can result in desirable lower reflectivity and higher absorption. Niziev and Nesterov [1999] analyzed the influence of beam polarization on laser cutting efficiency, and showed that beams with radial polarization are more effective in cutting and drilling than linearly polarized beams, whereas azimuthally polarized beams are very poor. This is because laser beams with azimuthal polarization are readily reflected whereas those with radial polarization are highly absorbed leading to more efficient cutting. Also, Quabis, Dorn, Eberler, Glöckl and Leuchs [2000] showed that radially polarized beams could be focused into smaller spots than linearly polarized beams (or azimuthally polarized beams). This is due to vectorial effects, and can be explained with the aid of fig. 42. With the linear polarization in fig. 42a, a partial cancellation of the field (destructive interference) between different parts of the beam occurs, whereas with the radial polarization shown in fig. 42b, all parts of the beam focus constructively to obtain a field which is essentially parallel to the optical axis. Youngworth and Brown [2000] performed some experiments on focusing of such beams, and the results agree with predictions.

§ 5. Concluding remarks

An important property in many applications is that the power of the laser output beams be as high as possible. In many cases, high powers can be obtained by resorting to lasers operating with a high-order mode, whose intensity distribution has a larger cross-section than the fundamental Gaussian mode, so it could more efficiently exploit the gain medium. Indeed, high powers were demonstrated either with lasers in which GRMs, DPEs or SPEs were inserted into the resonator, or with self-imaging resonators. Moreover, because spatial coherence of the beams emerging from such lasers is high, they could be efficiently transformed into a nearly Gaussian beam (see sect. 4.2). The use of intra-cavity mode shaping and single high-order mode selection, rather than external mode shaping, has two advantages. First, the laser output power is relatively high since a larger volume of the gain medium is exploited. Second, there is no need for external beam shaping, which introduces both additional losses and some distortions to the output intensity distributions.

When choosing between the different mode-selecting and mode-shaping methods, one should note that several methods are susceptible to small changes in the resonator, such as its length, or lensing properties of the gain medium (which can be caused by operating the laser with different pump powers). These include GPMs, diffractive elements and self-imaging or Fourier resonators, which are designed only for a specific set of parameters. Also, several methods are limited to specific resonator configurations. For example, self-imaging (Talbot) resonators are practical mainly for waveguide or slab-laser configurations and are significantly less efficient for other types of resonators; Fourier resonators require the existence of Fourier planes in the resonator; and some methods are specific to unstable resonators. Other methods are more general, and could be exploited in various resonator configurations and parameters.

Acknowledgements

The authors would like to thank the Pamot Venture Capital Fund and the Israeli Ministry of Science for their support.

References

Abramochkin, E.G., N. Losevsky and V.V. Volostnikov, 1997, Opt. Commun. **141**, 59.
Abrams, R.L., and A.N. Chester, 1974, Appl. Opt. **13**, 2117.

Abramski, K.M., H.J. Baker, A.D. Colley and D.R. Hall, 1992, Appl. Phys. Lett. **60**, 2469.
Ait-Ameur, K., 1993, J. Mod. Opt. **40**, 1833.
Angelow, G., F. Laeri and T. Tschudi, 1996, Opt. Lett. **21**, 1324.
Baker, H.J., D.R. Hall, A.M. Hornby, R.J. Morley, M.R. Taghizadeh and E.F. Yelden, 1996, IEEE J. Quantum Electron. **32**, 400.
Banerji, J., A.R. Davies and R.M. Jenkins, 1997, J. Opt. Soc. Am. B **14**, 2378.
Bastiaans, M.J., 1986, J. Opt. Soc. Am. A **3**, 1243.
Beijersbergen, M.W., R.P.C. Coerwinkel, M. Kristiansen and J.P. Woerdman, 1994, Opt. Commun. **112**, 321.
Bélanger, P.A., R.L. Lachance and C. Paré, 1992, Opt. Lett. **17**, 739.
Bélanger, P.A., and C. Paré, 1991, Opt. Lett. **16**, 1057.
Bélanger, P.A., and C. Paré, 1994, Opt. Commun. **109**, 507.
Borek, G.T., and D.R. Brown, 1999, SPIE Proc. **3633**, 51.
Born, M., and E. Wolf, 1965, Principles of Optics (Pergamon, Oxford) ch. 10.
Bourderionnet, J., N. Huot, A. Brignon and J.-P. Huignard, 2000, Opt. Lett. **25**, 1579.
Bourliaguet, B., A. Mugnier, V. Kermène, A. Barthélémy and C. Froehly, 1999, Opt. Commun. **167**, 177.
Bowers, M.S., 1992, Opt. Lett. **17**, 1319.
Bryngdahl, O., 1974, J. Opt. Soc. Am. **64**, 1092.
Casperson, L.W., 1976, Opt. Quantum Electron. **8**, 537.
Casperson, L.W., 1977, Opt. Quantum Electron. **9**, 499.
Casperson, L.W., N.K. Kincheloe and O.M. Stafsudd, 1977, Opt. Commun. **21**, 1.
Charters, R.B., B. Luther-Davies and F. Ladouceur, 1999, IEEE Photonics Tech. Lett. **11**, 1617.
Chen, D., Z. Wang and J.R. Leger, 1995, Opt. Lett. **20**, 663.
Cherezova, T.Y., S.S. Chesnokov, L.N. Kaptsov and A.V. Kudryashov, 1998a, Opt. Commun. **155**, 99.
Cherezova, T.Y., S.S. Chesnokov, L.N. Kaptsov and A.V. Kudryashov, 1998b, Opt. Exp. **3**, 180.
Courtial, J., D.A. Robertson, K. Dholakia, L. Allen and M.J. Padgett, 1998, Phys. Rev. Lett. **81**, 4828.
Cutolo, A., T. Isernia, I. Izzo, R. Pierri and L. Zeni, 1995, Appl. Opt. **34**, 7974.
Daschner, W., R. Stein, P. Long, C. Wu and S.H. Lee, 1996, SPIE Proc. **2689**, 153.
Davidson, N., A.A. Friesem and E. Hasman, 1992, Appl. Phys. Lett. **61**, 381.
Dragoman, D., 1997, Prog. Opt. **37**, 1.
Ehrlichmann, D., U. Habich and H.D. Plum, 1993, Appl. Opt. **32**, 6582.
Eppich, B., S. Johansson, H. Laabs and H. Weber, 2000, SPIE Proc. **3930**, 76.
Fox, A.G., and T. Li, 1962, Bell Syst. Tech. J. **40**, 453.
Gase, R., 1995, IEEE J. Quantum Electron. **31**, 1811.
Gerchberg, R.W., and W.O. Saxton, 1972, Optik **35**, 237.
Glova, A.F., N.N. Elkin, A.Y. Lysikov and A.P. Napartovich, 1996, Quantum. Electron. **26**, 614.
Graf, T., and J.E. Balmer, 1996, Opt. Commun. **131**, 77.
Harris, M., C.A. Hill, P.R. Tapster and J.M. Vaughan, 1994, Phys. Rev. A **49**, 3119.
Harris, M., C.A. Hill and J.M. Vaughan, 1994, Opt. Commun. **106**, 161.
Hasman, E., N. Davidson and A.A. Friesem, 1991, Opt. Lett. **16**, 423.
He, H., M.E.J. Friese, N.R. Heckenberg and H. Rubinsztein-Dunlop, 1995, Phys. Rev. Lett. **75**, 826.
Hodgson, N., T. Haase, R. Kostka and H. Weber, 1992, Opt. Quantum Electron. **24**, 927.
Hodgson, N., and H. Weber, 1997, Optical Resonators (Springer, Berlin) ch. 5.2.
Indebetouw, G., 1993, J. Opt. **24**, 3.
Jansen, M., J.J. Yang, S.S. Ou, D. Botez, J. Wilcox and L. Mawst, 1989, Appl. Phys. Lett. **55**, 1949.
Kermène, V., A. Saviot, M. Vampouille, B. Colombeau, C. Froehly and T. Dohnalik, 1992, Opt. Lett. **17**, 859.
Kogelnik, H., and T. Li, 1966, Proc. IEEE **54**, 1312.

Kol'chenko, A.P., A.G. Nikitenko and Y.K. Troitskii, 1980, Sov. J. Quantum Electron. **10**, 1013.
Kuga, T., Y. Torii, N. Shiokawa, T. Hirano, Y. Shimizu and H. Sasada, 1997, Phys. Rev. Lett. **78**, 4713.
Lapucci, A., and M. Ciofini, 1999, Appl. Opt. **38**, 4552.
Le Gall, J., and G.L. Bourdet, 1994, IEEE J. Quantum Electron. **30**, 1455.
Leger, J.R., D. Chen and K. Dai, 1994, Opt. Lett. **19**, 1976.
Leger, J.R., D. Chen and G. Mowry, 1995, Appl. Opt. **34**, 2498.
Leger, J.R., D. Chen and Z. Wang, 1994, Opt. Lett. **19**, 108.
Lescroart, G., and G. Bourdet, 1995, Opt. Commun. **119**, 373.
Lin, Q., and L. Wang, 2000, Opt. Commun. **175**, 295.
Liu, J., B.Y. Gu and G.Z. Yang, 1999, Appl. Opt. **38**, 6887.
Liu, Y., D. Cline and P. He, 1999, Nucl. Instrum. Methods A **424**, 296.
Makki, S., and J.R. Leger, 1999, IEEE J. Quantum Electron. **35**, 1075.
Makki, S., and J.R. Leger, 2001, IEEE J. Quantum Electron. **37**, 80.
Marhic, M.E., and E. Garmire, 1981, Appl. Phys. Lett. **38**, 743.
Massudi, R., and M. Piché, 1997, Opt. Commun. **142**, 61.
McDonald, G.S., G.P. Karman, G.H.C. New and J.P. Woerdman, 2000, J. Opt. Soc. Am. B **17**, 524.
Morin, M., 1997, Opt. Quantum Electron. **29**, 819.
Morley, R.J., E.F. Yelden, H.J. Baker and D.R. Hall, 1995, Appl. Opt. **34**, 418.
Murphy, J.B., 1999, Opt. Commun. **165**, 11.
Mushiake, Y., K. Matsumura and N. Nakajima, 1972, Proc. IEEE Lett. **60**, 1107.
Napartovich, A.A., N.N. Elkin, V.N. Troschieva, D.V. Vysotsky and J.R. Leger, 1999, Appl. Opt. **38**, 3025.
Nesterov, A.V., V.G. Niziev and V.P. Yakunin, 1999, J. Phys. D **32**, 2871.
Niziev, V.G., and A.V. Nesterov, 1999, J. Phys. D **32**, 1455.
Oron, R., S. Blit, N. Davidson, A.A. Friesem, Z. Bomzon and E. Hasman, 2000, Appl. Phys. Lett **77**, 3322.
Oron, R., Y. Danziger, N. Davidson, A.A. Friesem and E. Hasman, 1999a, Appl. Phys. Lett. **74**, 1373.
Oron, R., Y. Danziger, N. Davidson, A.A. Friesem and E. Hasman, 1999b, Opt. Commun. **169**, 115.
Oron, R., N. Davidson, A.A. Friesem and E. Hasman, 2000a, Opt. Lett. **25**, 939.
Oron, R., N. Davidson, A.A. Friesem and E. Hasman, 2000b, Opt. Commun. **182**, 205.
Oron, R., N. Davidson, A.A. Friesem and E. Hasman, 2001, Opt. Commun. **193**, 227.
Oron, R., L. Shimshi, S. Blit, N. Davidson, A.A. Friesem and E. Hasman, 2001, Opt. Lett. (submitted).
Pääkkönen, P., and J. Turunen, 1998, Opt. Commun. **156**, 359.
Paré, C., and P.A. Bélanger, 1992, IEEE J. Quantum Electron. **28**, 355.
Parent, A., M. Morin and P. Lavigne, 1992, Opt. Quantum Electron. **24**, S1071.
Piché, M., and D. Cantin, 1991, Opt. Lett. **16**, 1135.
Pohl, D., 1972, Appl. Phys. Lett. **20**, 266.
Quabis, S., R. Dorn, M. Eberler, O. Glöckl and G. Leuchs, 2000, Opt. Commun. **179**, 1.
Rigrod, W.W., 1963, Appl. Phys. Lett. **2**, 51.
Rioux, M., P.A. Bélanger and M. Cormier, 1977, Appl. Opt. **16**, 1791..
Saghafi, S., and C.J.R. Sheppard, 1998, Opt. Commun. **153**, 207.
Sanderson, R.L., and W. Streifer, 1969, Appl. Opt. **8**, 131.
Santarsiero, M., F. Gori, R. Borghi and G. Guattari, 1999, Appl. Opt. **38**, 5272.
Sato, S., Y. Harada and Y. Waseda, 1994, Opt. Lett. **19**, 1807.
Saviot, F., E. Mottay, M. Vampouille and B. Colombeau, 1993, Opt. Lett. **18**, 2117.
Sherstobitov, V.E., and A.Y. Rodionov, 2000, SPIE Proc. **3930**, 62.
Siegman, A.E., 1974, Appl. Opt. **13**, 353.

Siegman, A.E., 1986, Lasers (University Science Books, Sausalito, CA).
Siegman, A.E., 1990, SPIE Proc. **1224**, 2.
Siegman, A.E., 1993, Opt. Lett. **18**, 675.
Siegman, A.E., and H.Y. Miller, 1970, Appl. Opt. **9**, 2729.
Simon, R., and G.S. Agarwal, 2000, Opt. Lett. **25**, 1313.
Soskin, M.S., V.N. Gorshkov, M.V. Vasnetsov, J.T. Malos and N.R. Heckenberg, 1997, Phys. Rev. A **56**, 4064.
Stadler, M., and M. Schadt, 1996, Opt. Lett. **21**, 1948.
Suleski, T.J., and D.C. O'Shea, 1995, Appl. Opt. **34**, 7507.
Talbot, H.F., 1936, Philos. Mag. J. Sci. **9**, 401.
Tang, X.T., J. Xin and V.N. Ochkin, 1998, Opt. Eng. **37**, 266.
Tidwell, S.C., G.H. Kim and W.D. Kimura, 1993, Appl. Opt. **32**, 5222.
Tovar, A.A., 1998, J. Opt. Soc. Am. A **15**, 2705.
Tovar, A.A., and L.W. Casperson, 1998, J. Opt. Soc. Am. A **15**, 2425.
Tröbs, M., J.E. Balmer and T. Graf, 2000, Opt. Commun. **182**, 437.
Uehara, K., and H. Kikuchi, 1989, Appl. Phys. B **48**, 125.
Van Eijkelenborg, M.A., Å.M. Lindberg, M.S. Thijssen and J.P. Woerdman, 1998, IEEE J. Quantum Electron. **34**, 955.
Van Neste, R., C. Paré, R.L. Lachance and P.A. Bélanger, 1994, IEEE J. Quantum Electron. **30**, 2663.
Visser, T.D., A.T. Friberg and E. Wolf, 2001, Opt. Commun. **187**, 1.
Warnky, C.M., B.L. Anderson and C.A. Klein, 2000, Appl. Opt. **39**, 6109.
Wigner, E., 1932, Phys. Rev. **40**, 749.
Wolf, E., and G.S. Agarwal, 1984, J. Opt. Soc. Am. A **1**, 541.
Wolff, S., D. Messerschmidt and H. Fouckhardt, 1999, Opt. Exp. **5**, 32.
Wynne, J.J., 1974, IEEE J. Quantum Electron. **10**, 125.
Yariv, A., 1991, Optical Electronics (HRW, Philadelphia), ch. 2,4.
Youngworth, K., and T.G. Brown, 2000, Opt. Exp. **7**, 77.
Zeitner, U.D., F. Wyrowski and H. Zellmer, 2000, IEEE J. Quantum Electron. **36**, 1105.
Zhao, D., 1999, Optik **110**, 447.
Zhou, J.Y., C.H. Fu, Z.G. Lu, Q.X. Li and Z.X. Yu, 1991, Opt. Commun. **81**, 385.